

AD-A155 257

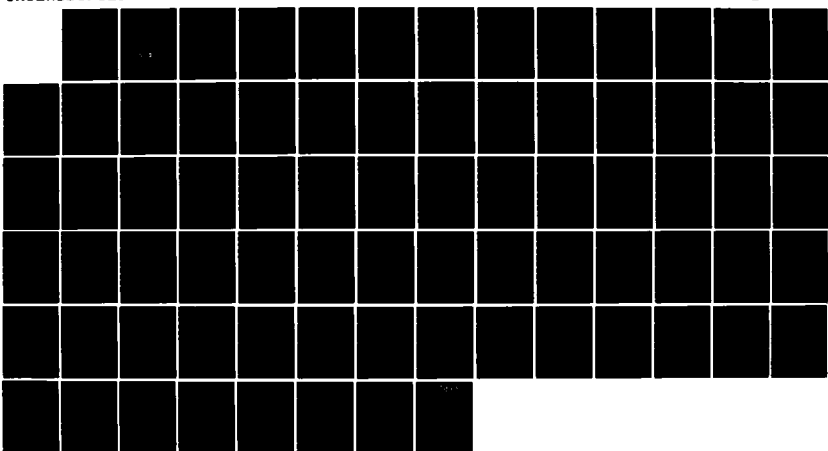
IONOSPHERIC ELECTRON DENSITY PROFILE AND RELATED  
STUDIES(U) BOSTON COLL CHESTNUT HILL MA SPACE DATA  
ANALYSIS LAB B BASU ET AL 15 AUG 84 AFGL-TR-84-0257

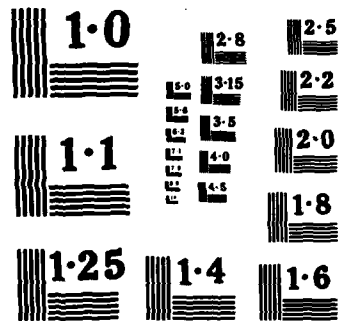
1/1

UNCLASSIFIED

F/G 4/1

NL





NATIONAL BUREAU OF STANDARDS  
MICROCOPY RESOLUTION TEST CHART

2  
JMK

IONOSPHERIC ELECTRON DENSITY PROFILE  
AND RELATED STUDIES

Bamandas Basu  
Dwight T. Decker  
John M. Rettner  
Pradip M. Bakshi

AD-A155 257

Space Data Analysis Laboratory  
Boston College  
Chestnut Hill, Massachusetts 02167

15 August 1984

Final Report  
1 October 1980 — 15 July 1984

Approved for Public Release, Distribution Unlimited



Air Force Geophysics Laboratory  
Air Force Systems Command  
United States Air Force  
Hanscom AFB, Massachusetts 01731

DTIC FILE COPY

85 5 17 04 4

"This technical report has been reviewed and is approved for publication"

*Milton M. Klein*  
MILTON M. KLEIN  
Contract Manager  
Ionospheric Effects Branch

*John A. Klobuchar*  
JOHN A. KLOBUCHAR, Acting Chief  
Ionospheric Effects Branch  
Ionospheric Physics Division

FOR THE COMMANDER

*Robert Skritvanek*  
ROBERT A. SKRIVANEK  
Director  
Ionospheric Physics Division

This report has been reviewed by the ESD Public Affairs Office (PA) and is releasable to the National Technical Information Service (NTIS).

Qualified requestors may obtain additional copies from the Defense Technical Information Center. All others should apply to the National Technical Information Service.

If your address has changed, or if you wish to be removed from the mailing list, or if the addressee is no longer employed by your organization, please notify AFGL/DAA, Hanscom AFB, MA 01731. This will assist us in maintaining a current mailing list.

Accession For	
NTIS GRAFI	
DTIC TAB	
Unannounced	
Justification	
By	
Distribution/	
Availability Codes	
Dist	Avail and/or Special
A/1	

NTIS GRAFI

DTIC TAB

Unannounced

Justification

By

Distribution/

Availability Codes

Dist

Avail and/or  
Special

A/1



## UNCLASSIFIED

SECURITY CLASSIFICATION OF THIS PAGE

## REPORT DOCUMENTATION PAGE

1a. REPORT SECURITY CLASSIFICATION Unclassified		1b. RESTRICTIVE MARKINGS									
2a. SECURITY CLASSIFICATION AUTHORITY		3. DISTRIBUTION/AVAILABILITY OF REPORT Approved for public release; distribution unlimited									
2b. DECLASSIFICATION/DOWNGRADING SCHEDULE											
4. PERFORMING ORGANIZATION REPORT NUMBER(S)		5. MONITORING ORGANIZATION REPORT NUMBER(S) AFGL-TR-84-0257									
6a. NAME OF PERFORMING ORGANIZATION Space Data Analysis Laboratory	6b. OFFICE SYMBOL (If applicable) BC-SDAL-84-2	7a. NAME OF MONITORING ORGANIZATION AFGL									
6c. ADDRESS (City, State and ZIP Code) Boston College Chestnut Hill, MA 02167		7b. ADDRESS (City, State and ZIP Code) Hanscom Air Force Base Bedford, MA 01731									
8a. NAME OF FUNDING/SPONSORING ORGANIZATION Air Force Geophysics Laboratory	8b. OFFICE SYMBOL (If applicable) LIS	9. PROCUREMENT INSTRUMENT IDENTIFICATION NUMBER F19628-81-K-0009									
8c. ADDRESS (City, State and ZIP Code) Hanscom AFB, MA 01731-5000 Monitor: Milton M. Klein		10. SOURCE OF FUNDING NOS. <table border="1"> <tr> <th>PROGRAM ELEMENT NO.</th> <th>PROJECT NO.</th> <th>TASK NO.</th> <th>WORK UNIT NO.</th> </tr> <tr> <td>62101F</td> <td>4643</td> <td>06</td> <td>BB</td> </tr> </table>		PROGRAM ELEMENT NO.	PROJECT NO.	TASK NO.	WORK UNIT NO.	62101F	4643	06	BB
PROGRAM ELEMENT NO.	PROJECT NO.	TASK NO.	WORK UNIT NO.								
62101F	4643	06	BB								
11. TITLE (Include Security Classification) Ionospheric Electron Density Profile and Related Studies											
12. PERSONAL AUTHOR(S) Basu, Bamandas, Decker, Dwight T., Retterer, John M., Bakshi, Pradip M.											
13a. TYPE OF REPORT Final	13b. TIME COVERED FROM 10-1-80 TO 7-15-84	14. DATE OF REPORT (Yr., Mo., Day) 84-8-15	15. PAGE COUNT 73								
16. SUPPLEMENTARY NOTATION											
17. COSATI CODES <table border="1"> <tr> <th>FIELD</th> <th>GROUP</th> <th>SUB. GR.</th> </tr> <tr> <td>0401</td> <td>20</td> <td>09</td> </tr> </table>		FIELD	GROUP	SUB. GR.	0401	20	09	18. SUBJECT TERMS (Continue on reverse if necessary and identify by block number) Photoelectron energy spectrum; upper hybrid instability; plasma instabilities electron cyclotron instability; lower hybrid frequency			
FIELD	GROUP	SUB. GR.									
0401	20	09									
19. ABSTRACT (Continue on reverse if necessary and identify by block number) In the daytime midlatitude lower ionosphere the primary source of electrons is photo-ionization of the neutral gas by photons in the extreme ultraviolet (EUV) region of the solar spectrum. We have studied this process in detail, along with the various particle-particle collisional processes that determine the energy dependence of the photoelectron flux. We have also studied the effects of plasma instabilities in determining the photo-electron energy spectrum in the 2-6 eV energy range.											
In circumstances where ionospheric sounders and other direct means cannot be used to determine the electron density profile (EDP) of the ionosphere, some means of modeling the EDP or determining it by remote sensing must be found. One useful diagnostic tool for EDP is the airglow emission. In this report, we describe a series of case studies, modeling the EDP using first-principle calculations and comparing the results to a variety of direct measurements. For cases in which simultaneous airglow emission measurements are available, we evaluate the emissions predicted by our model EDP and compare with the observed emissions.											
20. DISTRIBUTION/AVAILABILITY OF ABSTRACT UNCLASSIFIED/UNLIMITED <input checked="" type="checkbox"/> SAME AS RPT. <input type="checkbox"/> DTIC USERS <input type="checkbox"/>		21. ABSTRACT SECURITY CLASSIFICATION (CONT) Same as report									
22a. NAME OF RESPONSIBLE INDIVIDUAL Milton M. Klein		22b. TELEPHONE NUMBER (Include Area Code) 617-861-3137	22c. OFFICE SYMBOL AFGL/LIS								

UNCLASSIFIED

SECURITY CLASSIFICATION OF THIS PAGE

The nighttime ionosphere at high latitudes, i.e., in the auroral zone, is created by energetic particles precipitating from the magnetosphere. We have addressed the problem of specifying the flux incident on the atmosphere with a calculation of the magnetospheric loss-cone population resulting from pitch-angle diffusion. In an effort to describe the phenomena of ion conics, we have also studied both the means by which turbulence can be caused by precipitating electrons and the way in which the turbulence can accelerate ionospheric ions, using particle plasma simulation techniques.

An analysis has been made of the dependence of the potential of a charge emitting probe on beam current. A simplified analysis shows no dependence upon beam current for the spherical geometry and a weak dependence for the cylindrical case. A more extended analysis for a mixed geometry shows a weak dependence upon beam current. A comparison of the calculated results with experimental data indicates the calculated values are below the experimental values at low beam current and above at high beam currents. Possible improvements in the analysis by accounting for ion space charge, ion-trapping, etc., are indicated.

18. linear plasma theory	loss cone
electron density	particle precipitation
ion acceleration	curve-particle interaction
ion conics	Monte Carlo model
airglow emission	plasma simulation
probe potential	beam current
spacecraft charging	ion space charge

UNCLASSIFIED  
SECURITY CLASSIFICATION OF THIS PAGE

TABLE OF CONTENTS

<u>Section</u>		<u>Page</u>
	LIST OF ILLUSTRATIONS	v
	ACKNOWLEDGEMENTS	vii
I.	THEORY OF ELECTRON ENERGY DISTRIBUTION IN THE DAYTIME MIDLATITUDE IONOSPHERE	I-1
	I.1. Photoelectron Energy Spectrum	I-1
	I.1.1 High Energy Tail of the Photoelectron Distribution Function	I-1
	I.1.2 Photoelectron Distribution Function at Thermal and Near Thermal Energies	I-4
	I.2. Plasma Instabilities and Their Effects on the Photoelectron Energy Distribution	I-6
	I.2.1 Linear Theory of the Plasma Instabilities	I-7
	I.1.2.1 Upper Hybrid Instability	I-9
	I.1.2.2 Electron Cyclotron Instability	I-12
	I.2.2 Quasilinear Evolution of the Waves and of the Photoelectron Distribution	I-13
	References	I-18
II.	MODELING OF DAYTIME AIRGLOW AND ELECTRON DENSITY PROFILE IN THE MIDLATITUDE IONOSPHERE	II-1
	References	II-7
III.	PARTICLE PRECIPITATION: MAGNETOSPHERE-IONOSPHERE COUPLING	III-1
	III.1 The Loss-Cone Population in the Magnetosphere	III-2
	III.1.1 The Boundary-Layer Equation	III-3
	III.1.2 The Pitch-Angle Distribution	III-4
	III.1.3 Anisotropy in the Continuous Aurora	III-5
	III.1.4 Discussion	III-6
	III.2 Ion Acceleration in the Supraauroral Region	III-7
	III.2.1 The Formation of Ion Conics	III-9
	III.2.2 Discussion	III-10
	III.2.3 Conclusion	III-13
	References	III-14

TABLE OF CONTENTS (Cont.)

<u>Section</u>	<u>Page</u>
IV. PROBE THEORY	IV-1
IV.1 Introduction	IV-1
IV.2 Detailed Theory	IV-2
IV.2.1 Spherical Geometry	IV-3
IV.2.2 Cylindrical Geometry	IV-6
IV.2.3 Mixed Geometry	IV-7
IV.3 Comparison with Experiments	IV-7
References	IV-9

List of Illustrations

<u>Figure</u>		<u>Page</u>
I-1	Calculated [Ref. 1] and measured photoelectron flux in the 2-6 eV energy range at various altitudes in km.	I-19
II-1	White Sands Missile Range, August 23, 1972, calculated and observed electron density vs. altitude.	II-8
II-2	White Sands Missile Range, August 14, 1979, calculated and observed electron density vs. altitude.	II-9
II-3	ISIS-2 topside sounder, May 23, 1972, calculated and observed electron density vs. altitude.	II-10
II-4	Millstone incoherent scatter radar, April 8, 1978 calculated and observed electron density vs. altitude.	II-11
II-5	S3-4 satellite spectrometer, April 8, 1978, calculated and observed LBH bands and OI 1356 airglow vs. wavelengths.	II-12
II-6	S3-4 satellite spectrometer, April 8, 1978, calculated and observed OI 1356 airglow vs. latitude.	II-13
II-7	S3-4 satellite spectrometer, April 8, 1978, calculated and observed LBH 1383 A airglow vs. latitude.	II-14
II-8	Geometry of Hilat/Millstone coincidence, July 12, 1983.	II-15
II-9	AIM (Hilat) VUV imager, July 12, 1983, calculated and observed OI 1356 airglow vs. look direction given by pixel.	II-16
II-10	Millstone ionosonde July 12, 1983, calculated and observed electron density vs. altitude.	II-17
III-1	The boundary-layer, pitch-angle distribution at $\tau=1$ versus the pitch-angle variable for different values of $u_\ell$ . The arrows point to the edge of the loss cone in each case. The dashed curves give the logarithmic approximations from Eq. (8).	III-17
III-2	The pitch-angle distribution versus the pitch-angle variable at increasing values of the scattering-depth coordinate $\tau$ , corresponding to points ranging from one footpoint of the geomagnetic field line to the other. Inset: The pitch-angle distribution in the two loss cones at one point in space. For this polar plot of the pitch-angle distribution at fixed energy, we have scaled values of pitch angle from values of $u$ assuming that the half angle of the loss cone is $45^\circ$ for the sake of illustration.	III-18

List of Illustrations (Cont.)

<u>Figure</u>		<u>Page</u>
III-3	Electron flux versus normalized pitch angle at six energies (in keV), from the ISIS-2 data at $\Lambda=68.6^\circ$ , at 0610 UT on December 9, 1971. The smooth curves are theoretical pitch-angle distributions, fitted to the data by eye.	III-19
III-4	Bounce-averaged diffusion coefficient versus invariant latitude at three energies.	III-20
III-5	The ion conic in two regions. LH acceleration of $H^+$ occurs over the range from 1000 to 2000 km in this simulation, with $E_w = 50$ mV/m. The lower panel gives the conic at the edge of the acceleration region, 2000 km, while the upper panel gives the conic folded by the geomagnetic field at an altitude 3000 km. To give reasonable statistics, the particles from an altitude interval of 1000 km below the observation point are included in each panel, with their velocities adiabatically folded to the observation altitude.	III-21
III-6	The energy distribution of accelerated ions. The solid line gives the result with a constant diffusion coefficient, while the dashed (dotted) line gives the result with a resonance limit at 1 keV (500 eV). The diffusion coefficient is constant up to this energy, and then falls as $v_\perp^{-3}$ with increasing energy. The calculation of the distribution function includes all particles above 2000 km in the simulation of Fig. 1. The normalization of $F(E)$ is arbitrary.	III-22

ACKNOWLEDGEMENTS

The authors wish to thank Mr. Leo F. Power, Jr., the Director of the Space Data Analysis Laboratory, for his able administrative assistance throughout the duration of this contract.

Special thanks go to Mr. Neil Grossbard of the laboratory for his programming and analysis efforts.

To the Contract Monitor, Dr. Milton Klein, thanks are extended for his collaboration and assistance.

We wish to thank Miss Mary Kelly for an excellent job in typing this document, and for her suggestions in improving the presentation.

### I.1. Photoelectron Energy Spectrum

In the daytime midlatitude lower ionosphere the primary source of electrons is photoionization of the neutral gas by photons in the extreme ultraviolet (EUV) region of the solar spectrum. We have studied this process in detail along with the various particle-particle collisional processes that determine the energy dependence of the photoelectron flux. Our analysis is based on Boltzmann-Fokker-Planck theory in the local approximation as developed by Jasperse<sup>1</sup>.

Using this theory we can calculate the isotropic electron distribution function (EDF) from a detailed balance equation of electron sources and sinks in phase space. The equation in energy space is

$$0 = \frac{\delta F_0(E)}{\delta t} \Big|_{p_1} + \frac{\delta F_0(E)}{\delta t} \Big|_{\text{coll}} \quad (1)$$

where the terms on the right-hand side are given in Jasperse<sup>2,3</sup>. The two general features of the EDF are a Maxwellian in the thermal region with a structured and inflated tail at high energies (1-200 eV). The electrons are generally produced at high energies by photons ionizing the neutrals. These photoelectrons then lose energy through both electron conserving and electron producing collisions and eventually attain "thermal" energies where recombination with ions becomes an effective sink.

In I.1.1, we discuss the detailed processes that lead to the high energy tail of the EDF. In Section B, we focus on the role of the electron-electron collisions in the transition region of near-thermal energies where the EDF changes character from a tail-like structure to a Maxwellian.

#### I.1.1. High Energy Tail of the Photoelectron Distribution Function

In the photoionization process, a neutral particle absorbs a photon of energy  $h\nu$  and an electron is ejected with energy  $E = h\nu - E_{pijm}$ , where  $E_{pijm}$  is the ionization energy associated with the ionization process in which the neutral  $j$  is transformed into an ion in state  $m$ . The number of electrons with energy  $E$  produced by such a process is

$$I(E+E_{pijm}) Q_{pijm}(E+E_{pijm}) n_j , \quad (2)$$

where  $I$  is the number of photons with energy  $h\nu=E+E_{pijm}$ ,  $Q_{pijm}$  is the cross-section for the photoionization process described above, and  $n_j$  is the density of neutral  $j$ . To calculate the total electron production rate due to a photon of energy  $h\nu$  one has to sum over all the neutral species and all the final ionic states. In our initial modeling we included contributions from 20 of the electronic bound and dissociating states of  $O^+$ ,  $N_2^+$  and  $O_2^+$ .

The solar EUV spectrum is highly structured being composed primarily of narrow lines<sup>4</sup> with the largest line being He II (40.7 eV) with a measured width (FWHM) of .013 eV. From formula 2, it is clear that if the cross section is reasonably constant over the width of a solar line then such a narrow line at  $h\nu$  will lead to a narrow peak in the photoelectron production spectrum at  $h\nu-E_{pijm}$ . Such a production peak is then degraded by various interactions in the plasma resulting in shifted, reduced and smeared peaks in the photoelectron spectrum. Such structure has been seen in measured photoelectron spectrum<sup>5</sup>, particularly between 20 to 30 eV where several large peaks can be identified with the photoionization [of  $O_2$  and  $N_2$ ] by the He II line.

In spite of the particle interactions much of the structure in the photoelectron spectrum can be directly identified with a specific solar line, neutral specie and final ion state. The four major peaks of the photoelectron spectrum form a definite pattern determined by threshold energies for producing  $N_2^+$  and  $O_2^+$  in their ground, first excited and second excited states. While the He II (40.8 eV) solar line produces the largest version of the pattern between 21 and 28 eV strong solar lines at 33.6 eV and 48.2 eV produce the same pattern simply shifted in the photoelectron spectrum by the energy difference between these solar lines and the HE II line. The pattern is not limited to four peaks but is part of a larger pattern which includes the photoproduction of other ionic states by a particular solar line.

While we can identify some of the structure in the photoelectron spectrum as arising directly from photoionization there is another process which contributes significantly to the structure, namely, electron-neutral inelastic scattering. In inelastic scattering the electrons of the photoionization peaks scatter off the neutrals and lose discrete amounts of energy resulting in shifted peaks which are reduced images of the photoionization peaks. With these two processes, photoionization and electron neutral inelastic scattering, we

found excellent agreement with satellite data with respect to the locations of peaks and the general character of the photoelectron spectrum.

While we included such interactions as electron-electron and electron-neutral to account for the degradation of the production peaks a variety of effects which would broaden a peak during the photoionization process were neglected. To account for this the solar lines were given an increased width, 2 eV for HE II, where the width was on the same order as the vibrational spacing for the molecules. This ad hoc width fundamentally determined the width and shape of the peaks in the photoelectron spectrum. While our agreement with data was generally excellent the widths of the theoretical peaks were less than the observed widths. Before one can consider if other processes such as wave-particle interactions could be important it is necessary to first consider the photoionization process in greater detail.

We have found that the effects in photoionization due to natural line broadening, Doppler broadening, pressure broadening, molecular rotation levels and atomic fine structure are of the same order or smaller than the experimental widths of the solar lines. From photoelectron spectroscopy data<sup>6</sup> we have seen that enough of the vibrational levels of a given molecular electronic bound state can be populated so as to cause a spread in electron energy as large as 4.94 eV. We include these facts in our modeling by, first, using a solar spectrum with line width (.04 eV for HE I) of the order of the measured solar line widths and, second, explicitly including the molecular vibration levels in the photionization process.

Inclusion of vibrational effects changes Eq. (2) in the following manner

$$I(h\nu) B_{n jm}(h\nu) Q_{pi jm}(h\nu) n_j \quad (3)$$

where  $B_{n jm}$ 's are branching ratios for the vibrational states for an electronic state  $jm^7$ . The electron energy  $E$  is now given as  $E=h\nu-E_{pi jm}-\Delta E_{nvib}$  so that the number of photoelectron peaks from a particular solar line and molecular state  $jm$  equals the number of vibrational levels of state  $jm$  that are populated. In our current modeling we have included branching ratios for 8 of the  $O_2^+$  and  $N_2^+$  electronic states.

These modifications broaden the theoretical widths and remove the ad-hoc nature of our previous calculations. The energy resolution of present photoelectron data is such that it is difficult to quantify what differences remain

between theoretical and experimental widths. It does appear though that theory may still underestimate the broadening of photoelectron peaks. Theoretically the next step is to include the interactions of electrons with the thermal wave fluctuations. Experimentally, high resolution measurements of the tail of the EDF would clearly quantify differences between any theoretical modeling and data.

### I.1.2. Photoelectron Distribution Function at Thermal and Near Thermal Energies

In recent years there has been increased interest in the thermal and near thermal energy regions of the photoelectron distribution function. In theoretical calculations of the EDF how one treats the electron-electron interactions (at these energies) is an important concern. From an examination of our solutions of Eq. (1) and the various processes involved at low energies we have come to some conclusions concerning how the electron-electron interactions should be treated.

We used the Fokker-Planck description for the Coulomb collisions between electrons

$$\frac{\Delta F(\bar{v}, t)}{\delta T_{ee}} = \bar{v} \cdot [-f(\bar{v}, t) (\Delta \bar{v})_{av} + \frac{1}{2} \nabla \cdot f(\bar{v}, t) (\Delta \bar{v} \Delta \bar{v})_{av}] . \quad (4)$$

The first term is called the dynamical friction term and the second is the velocity diffusion term. The friction term describes the tendency of electron-electron collisions to act as a force accelerating or decelerating electrons to the average velocity. The diffusion term describes the tendency of the collisions to diffuse the electrons out in velocity space so there are random fluctuations about the average velocity. A Maxwellian distribution of electrons represents a distribution where these two effects exactly balance.

Our calculation, done in energy space following the Rosenbluth, MacDonald and Judd<sup>8</sup> development and involving the integral of the kinetic equation, gives

$$4\pi \int_E^\infty \frac{\delta F_0}{\delta T_{ee}} dE = -k_{ee} (I_0^0 - J_{-1}^0) \frac{4\pi F}{E^{1/2}} - 4\pi k_{ee} \frac{\partial}{\partial E} \left( \frac{2}{3} E^{1/2} (I_2^0 + J_{-1}^0) F_0 \right) \quad (5)$$

where

$$I_0^0 = 4\pi \int_0^E F(x) dx, \quad I_2^0 = \frac{4\pi}{E} \int_0^E xF(x) dx, \quad J_{-1}^0 = 4\pi E^{1/2} \int_E^\infty dx \frac{F(x)}{x^{1/2}}$$

and  $k_{ee} = 2\left(\frac{m}{2}\right)^{3/2} 4\pi \left(\frac{e^2}{m}\right) \ln\Lambda$ . The first term we still label friction and the second diffusion. Further, the average energy loss rate for an electron is

$$\frac{-k_{ee}(I_0^0 - J_{-1}^0)}{E^{1/2}}$$

which in the case of having  $F(x)$  a Maxwellian in  $I_0^0$ ,  $I_2^0$  and  $J_{-1}^0$  agrees with the Butler and Buckingham energy loss rate.<sup>9</sup> It is some form of friction term which is used in most calculations of the photoelectron distribution function while the diffusion term is often neglected.

The use of a friction term can be justified in general for high energy where fast electrons are decelerated towards thermal regions. The two exceptions where ignoring diffusion can be a problem are (1) near any sharp peaks where derivatives of  $F_0$  can be large and the proper description of the spreading of the peaks may require diffusion and 2) in the thermal and near thermal regions where the  $F$  is or is becoming Maxwellian in character so that the very existence of the Maxwellian indicates that friction and diffusion are of equal importance.

[From our calculations] we have seen [in 3 ways] the importance of the diffusion term. First, a comparison of our full solution to a simpler CSD solution. The CSD solution is an example of a calculation where only a friction type term is used, and we find that while it follows the high energy tail without peaks that at thermal and near thermal energies it contains none of the Maxwellian character of the full distribution function. Second, we did runs with the diffusion term turned off above various threshold energies. When the threshold was above 10KT away from the Maxwellian the solution was little affected. As the threshold was lowered below 10KT into the Maxwellian region the Maxwellian character above the threshold was completely lost and the electron temperature became radically wrong. Finally we were able to examine term by term the various processes included in our calculations. We found directly that at high energies the friction term is generally much larger than the diffusion term, but as one goes down to near thermal energies,  $10 K_{Te}$ , the diffusion term becomes of the same order as the friction term, but opposite sign. Further the two electron terms together do not dominate over the other processes of these energies, but the friction term alone dominates the other processes so

that, if the diffusion term is not there to cancel with it, a large error would be introduced in the equation.

Our basic conclusion is that the Maxwellian forms a natural boundary where one should use both friction and diffusion to describe the electron-electron interaction. In other words if one is concerned with the lower energies in the transition region between the Maxwellian and the high energy tail then electron-electron diffusion effect should be considered along with electron-electron friction. Recent work<sup>10</sup> has further confirmed the impact of and need for both types of terms in the calculation of the thermal electron heating rates.

## I.2. Plasma Instabilities and Their Effects on the Photoelectron Energy Distribution

One interesting feature of the theoretically calculated<sup>1</sup> photoelectron energy distribution, which is in disagreement with the measurements, occurs in the 2-6 eV energy range. In this energy range the distribution function has a minimum at about 2.3 eV (Fig. I-1). This is explained theoretically, since the cross section for the electron-impact excitation of vibrational states of N<sub>2</sub> has a maximum at 2.3 eV. Beyond 2.3 eV, the photoelectron flux rises sharply to a maximum at about 5 eV, as the excitation cross section decreases sharply. Beyond this energy the flux falls off as the cross section for the excitation of metastable states of atomic oxygen increases. The theoretical calculations (Fig. I-1) show that this minimum in the spectrum is more and more pronounced at or below altitudes of 130 km. Above 130 km, the valley starts to be filled up, the peak-to-valley ratio decreases, until at or above 210 km the structure disappears completely. This disappearance can be attributed to the depletion of N<sub>2</sub> as well as to the gradual smoothing process arising from electron-electron collisions as the altitude increases.

Measurements of the electron energy distribution by McMahon and Heroux<sup>11</sup>, who studied specifically the 2-5 eV energy range with improved energy resolution of the apparatus, are in good agreement with the theoretical calculations of Jasperse<sup>1</sup> at and above 170 km. Below 170 km, the calculated values of the peak-to-valley ratios by Jasperse<sup>1</sup> is larger than the measured values. The measurements are in most striking disagreement with the theory below 130 km, where they show plateaus in the distribution functions in the 2-5 eV energy range.

This discrepancy between theory and measurement suggests that in the low altitude regions (100-170 km) collisional processes alone cannot explain the observed photoelectron distributions. It is well-known that a homogeneous plasma in a magnetic field with isotropic distribution functions can be unstable if a population of high energy particles is also present. This is precisely the situation in the lower ionosphere, and it can be expected that the plasma instability will produce the anomalous diffusion in the velocity space through wave-particle interaction, which in turn will flatten the distribution functions in the 2-5 eV energy range. With this in mind, we studied excitation of electrostatic instabilities in the ionospheric collisional plasma by the suprathermal electrons near the 5-eV maximum.

Using the Bhatnagar-Gross-Krook (BGK) collision operator to take into account the effects of electron-neutral collisions, we find that the suprathermal electrons near 5 eV can excite electron cyclotron modes in the 110-130 km region, and upper hybrid modes above 125 km<sup>12</sup>. As the waves grow in amplitude at the expense of the suprathermal electron energy, growth rates are reduced. Eventually, a steady-state is reached in which the waves saturate to a finite level of amplitude and the electron energy distribution in the 2-6 eV energy range is considerably modified through anomalous diffusion in velocity space. We have studied these wave-particle effects within the framework of the so-called quasilinear theory of plasma turbulence.

In this section, we first discuss the linear theory of the plasma instabilities mentioned above. We then present the relevant quasilinear equations and discuss the approximate analytic solutions of these equations, showing the time evolutions of the electron distribution function and the wave spectral energy density from their initial to the time-asymptotic values.

#### 1.2.1. Linear Theory of the Plasma Instabilities

The equation for the one particle photoelectron distribution function,  $f$ , is

$$\left\{ \frac{\partial}{\partial t} + \underline{v} \cdot \frac{\partial}{\partial \underline{r}} - \frac{q}{m} [\underline{E} + (\underline{v} \times \underline{B}_0)/c] \cdot \frac{\partial}{\partial \underline{v}} \right\} f = S + L(f) , \quad (6)$$

where  $B_0$  is the geomagnetic field (assumed to be uniform),  $S$  is the photoelectron source function, and  $L$  is the total collision operator for electron-neutral, electron-electron and electron-ion collisions. The other quantities

have their usual meanings. We imagine that the equilibrium electron population is composed of a Maxwellian part and a suprathermal part, denoted by the two values of the subscript  $j$ , and study electrostatic perturbations from this equilibrium having frequencies  $\omega^2 \omega_p$ , where  $\omega_p$  is the electron plasma frequency. At these frequencies the ion dynamics can be ignored. We seek solutions of the form

$$f_j = f_{0j}(v) + f_{1j}(\underline{r}, \underline{v}, t) , \quad (7)$$

$$\underline{E} = 0 + \underline{E}_1(\underline{r}, \underline{v}, t) \quad (8)$$

where  $f_{0j}$  is the equilibrium (isotropic) distribution of the  $j$  type electrons,  $f_{1j}$  is the corresponding small amplitude perturbation, and  $\underline{E}_1$  is the perturbed electric field. Approximately decoupling the thermal from the suprathermal populations we find that the zero order equations are

$$0 = S + L(f_{0j}) , \quad (9)$$

and the first order equations are

$$\begin{aligned} & \left[ \frac{\partial}{\partial t} + \underline{v} \cdot \frac{\partial}{\partial \underline{r}} - \frac{q}{mc} (\underline{v} \times \underline{B}_0) \cdot \frac{\partial}{\partial \underline{v}} \right] f_{1j} \\ & - \frac{q}{m} \underline{E}_1 \cdot \frac{\partial}{\partial \underline{v}} f_{0j} = L(f_{0j} + f_{1j}) - L(f_{0j}) , \end{aligned} \quad (10)$$

$$\frac{\partial}{\partial \underline{r}} \cdot \underline{E}_1 = -4\pi q \sum \int d^3v f_{1j} . \quad (11)$$

It can be shown that  $L$  may be approximated by the BGK operator for the dominant electron-neutral collisions, i.e.,

$$\text{R.H.S. of (10)} \approx -v_j f_{1j} + v_j (n_{1j}/n_{0j}) f_{0j} , \quad (12)$$

where  $n_{0j}$  and  $n_{1j}(\underline{r}, t)$  are the equilibrium and perturbed densities, respectively. In (12)  $v_m$ , where  $j=m$  denotes the Maxwellian electrons, is approximately the elastic collision frequency, and  $v_h$  is the sum of the elastic and vibrational excitation collision frequency for the suprathermal electrons. The important point to note is that the Maxwellian, not the suprathermal, electrons are effective in damping the waves, and that (12) is a good approximate operator for the study of damping effects.

Assuming perturbations of the form  $\exp(i\underline{k} \cdot \underline{r} - i\omega t)$  we solve Eq. (10) for  $f_{1j}$  and then, with the aid of Eq. (11), obtain the dispersion relation

$$1 + (\omega_p^2/\Omega^2) \sum_j (N_j/D_j) = 0 , \quad (13)$$

where

$$N_j = \frac{\Omega^2}{k^2} \sum_{n=-\infty}^{\infty} \int d^3v \frac{J_n^2(k_{\perp}v_{\perp}/\Omega)}{\omega + iv_j - k_{\parallel}v_{\parallel} - n\Omega} \times \left( \frac{n\Omega}{v_{\perp}} \frac{\partial}{\partial v_{\perp}} + k_{\parallel} \frac{\partial}{\partial v_{\parallel}} \right) \beta_j g_{0j} , \quad (14)$$

$$D_j = 1 - iv_j \sum_{n=-\infty}^{\infty} \int d^3v \frac{J_n^2(k_{\perp}v_{\perp}/\Omega)}{\omega + iv_j - k_{\parallel}v_{\parallel} - n\Omega} g_{0j} . \quad (15)$$

Here  $\Omega = qB_0/mc$  is the electron cyclotron frequency,  $\omega_p^2 = 4\pi q^2 n_0/m$ , where  $n_0 = \sum_j n_{0j}$ ,  $g_{0j} = f_{0j}/n_{0j}$ ,  $\beta_j = n_{0j}/n_0$ ,  $k^2 = k_{\perp}^2 + k_{\parallel}^2$ , and other quantities have their usual meanings. For the Maxwellian electrons with density  $n_{0m}$  and temperature  $T_e$ , the velocity space integrations can be carried out and Eq. (13) becomes

$$1 - \frac{\omega_{pm}^2 k_{\parallel}^2}{\omega(\omega + iv_m)k^2} I_0 \exp(-b) - \sum_{n=1}^{\infty} \frac{2a_n n^2 \omega_{pm}^2 k_{\perp}^2 (\omega + iv_m)}{\omega[(\omega + iv_m)^2 - n^2 \Omega^2] k^2} + (\omega_p^2/\Omega^2) (N_h/D_h) = 0 . \quad (16)$$

Here  $a_n = (I_n/b) \exp(-b)$ ,  $I_n(b)$  is the modified Bessel function of the first kind,  $b = k_{\perp}^2 T_e/m \Omega^2$ ,  $\omega_{pm}^2 = 4\pi q^2 n_{0m}/m$ . We have assumed  $k_{\parallel}^2 \ll k_{\perp}^2$ , and  $(\omega - n\Omega)/[|k_{\parallel}|(2T_e/m)^{1/2}] \gg 1$  for all  $n$ , so that Landau damping and cyclotron damping can be neglected.

#### I.1.2.1 Upper Hybrid Instability

In the lower ionosphere we may assume  $b \ll 1$ , and  $\Omega^2/\omega_p^2 \ll 1$ . Without the suprathermal electron term, one of the roots ( $\omega = \omega_r + i\omega_c$ ,  $\omega_c \ll \omega_r$ ) of the dispersion equation (16) is

$$\omega_r = (\omega_{pm}^2 + \Omega^2)^{1/2} , \quad (17)$$

which is the upper hybrid frequency, and

$$\omega_c \approx - [(\omega_{pm}^2 + \Omega^2)/2\omega_r^2] v_m , \quad (18)$$

is the collisional damping rate.

The suprathermal electrons interact resonantly with the upper hybrid wave and drive it unstable, the resonance condition being  $\omega_r - k_{\parallel} v_{\parallel} = n\Omega$ . Since  $n_{oh} \ll n_{om}$ , the growth rate  $\gamma$  can be assumed to be small compared to  $\omega_r$  and is given by

$$\gamma \approx \frac{\pi^2 \omega_p^4}{k_{\perp}^2 |k_{\parallel}|} \left( \frac{n_{oh}}{n_{om}} \right) \sum_{n=-\infty}^{+\infty} \int_0^{\infty} dv_{\perp} J_n^2 \left( \frac{k_{\perp} v_{\perp}}{\Omega} \right) \left( \frac{\partial g_{oh}}{\partial v_{\perp}} \right) v_{\parallel} = (\omega_r - n\Omega)/k_{\parallel} . \quad (19)$$

The collisions of the suprathermal electrons will somewhat detune their resonance with the wave and reduce the growth rate. This damping rate can be shown to be  $\sim (n_{oh}/n_{om}) v_h$ . So, the significant damping is that due to the Maxwellian electrons and is given by Eq. (18). The explicit expression for  $\gamma$  in the energy representation using  $G_{oh}(E) = (2^{1/2} E^{1/2}/m^{3/2}) g_{oh}(v)$ , so that  $4\pi \int dE G_{oh} = 1$ , is

$$\gamma = \frac{\pi^2}{2} \left( \frac{n_{oh}}{n_{om}} \right) \left( \frac{\omega_p}{\Omega} \right)^4 \left( \frac{\Omega E_0^{1/2}}{|K_{\parallel}|} \right) \sum_{n=-\infty}^{+\infty} \int_{E_n}^{\infty} \frac{dE}{E^{1/2}} \times \frac{J_{n+1}^2(\alpha_n) - J_{n-1}^2(\alpha_n)}{n} G_{oh}(E) , \quad (20)$$

Here  $E_0 = mv_0^2/2$  is the peak energy ( $\approx 5$  eV) of the suprathermal electrons,  $K_{\parallel} = k_{\parallel} v_0 / \Omega$ ,  $E_n = E_0 [(\omega_r / \Omega - n) / K_{\parallel}]^2$ , and  $\alpha_n = (k_{\perp} v_0 / \Omega) [(E - E_n) / E_0]^{1/2}$ . We notice that  $\gamma$  depends on the parameters:  $n_{oh}/n_{om}$ ,  $\omega_p/\Omega$ ,  $k_{\parallel}$ , and  $k_{\perp}$ , which are altitude dependent. At a given altitude the unstable spectrum is given by the condition  $J_{n+1}^2 - J_{n-1}^2 > 0$ .

Numerical values of  $\gamma$  at various altitudes have been obtained using the energy distributions of Jasperse<sup>1</sup>, and the results are given in Table 1. The upper hybrid instability can be excited at an altitude as low as 125 km, below which it is stabilized by the collisions. Above 170 km, the damping effects of electron-electron and electron-ion collisions must be considered.

TABLE I. Values of Upper Hybrid Frequency ( $\omega_H$ ), Suprathermal Electron Abundance ( $\sigma$ ), Elastic Collision Frequency of Maxwellian Electrons ( $\nu_m$ ), Collisional Damping Rate ( $\omega_0$ ), Maximum Collisionless Growth Rate ( $\gamma_m$ ), Corresponding Perpendicular Wavelength ( $\lambda$ ) and  $k_{\perp}/k_{\parallel}$  as a Function of Altitude for  $B_0=0.35G$

Altitude (km)	$\omega_H (s^{-1})$	$\sigma = n_{\text{oh}}/n_{\text{om}}$	$\nu_m (s^{-1})$	$\omega_0 (s^{-1})$	$\gamma_m (s^{-1})$	$\lambda (cm)$	$k_{\perp}/k_{\parallel}$
125	$2.88 \times 10^7$	$2.3 \times 10^{-5}$	$8.0 \times 10^2$	$4.2 \times 10^2$	$4.4 \times 10^2$	15.4	23.8
140	$3.1 \times 10^7$	$1.3 \times 10^{-4}$	$4.0 \times 10^2$	$2.1 \times 10^2$	$1.73 \times 10^3$	11.9	57.0
170	$3.5 \times 10^7$	$3.7 \times 10^{-4}$	$1.36 \times 10^2$	$0.7 \times 10^2$	$2.71 \times 10^3$	10.8	17.7

### I.1.2.2 Electron Cyclotron Instability

Here we consider waves with  $k_{\parallel}=0$ , and the instability that is found is of the nonresonant type with  $\omega_r \approx n\Omega$ . In this case we can write

$$N_h \approx - \frac{8\pi\Omega^2\sigma}{k_{\perp}^2} \sum_{n=1}^{\infty} \frac{n^2\Omega^2}{(\omega+i\nu_h)^2-n^2\Omega^2} \times \int_0^{\infty} dv J_{2n} \left(\frac{2k_{\perp}v}{\Omega}\right) g_{oh}(v) , \quad (21)$$

$$D_h = 1 - \frac{4\pi\Omega}{k_{\perp}} \sum_{n=-\infty}^{+\infty} \frac{i\nu_h}{\omega+i\nu_h-n\Omega} \times \int_0^{\infty} dv v g_{oh} \sum_{p=0}^{\infty} J_{2n+2p+1} \left(\frac{2k_{\perp}v}{\Omega}\right) , \quad (22)$$

where  $\sigma = n_{oh}/n_{om} \approx \beta_h$ , and  $v^2 = v_{\perp}^2 + v_{\parallel}^2$ . We first solve Eq. (16) with  $k_{\parallel}=0$  in the limit  $v_m=0$ . We substitute  $\omega = n\Omega(1+\chi)$ , where  $n \geq 2$  and  $\chi \ll 1$ , and obtain

$$1 - \frac{2\omega_p^2 a_1}{(n^2-1)\Omega^2} + \frac{4n^2 \omega_p^2 a_1 \chi}{(n^2-1)^2 \Omega^2} - \frac{\omega_p^2}{\Omega^2 \chi} (a_n + \frac{\sigma I}{K_{\perp}^2}) = 0 , \quad (23)$$

where  $K_{\perp} = k_{\perp} v_0 / \Omega$ ,  $\omega_p^2 \approx \omega_{pm}^2$ , and

$$I = 4\pi E_0 \int_0^{\infty} \frac{dE}{E} G_{oh}(E) J_{2n} [2K_{\perp}(E/E_0)^{1/2}] \quad (24)$$

in the energy representation. We have neglected terms of the order of  $(\nu_h/\Omega) \sigma$  or smaller. It is readily seen that  $\chi$  will have a positive imaginary part (meaning instability) if  $I < 0$ ,  $|I| > a_n K_{\perp}^2 / \sigma$ , and

$$\left| 1 - \frac{2a_1\omega_p^2}{(n^2-1)\Omega^2} \right| < \frac{4n\omega_p^2 a_1^{1/2}}{(n^2-1)\Omega^2} \left( \frac{\sigma|I|}{K_1^2} - a_n \right)^{1/2} . \quad (25)$$

Condition (25) determines the range of values of  $\omega_p^2/\Omega^2$  for which the n-th harmonic can be unstable. The maximum values of  $\text{Im}\chi$  is obtained when  $\omega_p^2/\Omega^2 = (n^2-1)2a_1$ . In this case  $\chi$  is given by

$$\chi = i \frac{n^2-1}{nK_1} \left[ \frac{\sigma}{4a_1} \left( |I| - \frac{a_n K_1^2}{\sigma} \right) \right]^{1/2} . \quad (26)$$

The second term within the parentheses represents the finite-b stabilizing effect. In the presence of collisions ( $v_m \neq 0$ ), the complete solution of the dispersion relation is

$$\omega = n\Omega + i \left[ \gamma - \frac{(n^2+1)v_m}{4n^2} \right] , \quad n \geq 2 , \quad (27)$$

where  $\gamma = n\Omega(\text{Im}\chi)$  and the additional term is the collisional damping rate.

The electron cyclotron instability has a larger growth rate than that of the upper hybrid, and an unstable harmonic is localized within a narrow range ( $\sim 2$  km) around the altitude at which it has the maximum growth rate. Results of numerical calculations are summarized in Table 2. At altitudes 100 km and below, the mode is stabilized by the electron-neutral collisions while above 130 km it is stabilized by the finite-b effect.

#### I.2.2. Quasilinear Evolution of the Waves and of the Photoelectron Distribution

We have studied the upper hybrid waves analytically in somewhat details. Excitation of these waves requires resonant interaction between the suprathermal electrons and the wave, and the resonant diffusion, in velocity space, of the equilibrium suprathermal electrons in response to the unstable waves is governed by the following equation:

TABLE 2. Values of Cyclotron Harmonic Number ( $n$ ), Suprathermal Electron Abundance ( $\sigma$ ), Elastic Collision Frequency of Maxwellian Electrons ( $v_m$ ), Collisional Damping Rate ( $\omega_0$ ), Maximum Collisionless Growth Rate ( $\gamma_m$ ), and Corresponding Wavelength ( $\lambda$ ) as a Function of Altitude for  $B_0 = 0.35G$

Altitude (km)	$\omega/\Omega = n$	$\sigma = n_{oh}/n_{om}$	$v_m (s^{-1})$	$\omega_0 (s^{-1})$	$\gamma_m (s^{-1})$	$\lambda (cm)$
~100	3	$3.0 \times 10^{-6}$	$1.4 \times 10^4$	$3.89 \times 10^3$	$1.11 \times 10^3$	23.4
~110	4	$2.05 \times 10^{-5}$	$3.17 \times 10^3$	$7.43 \times 10^2$	$4.18 \times 10^3$	19.5
~130	5	$4.5 \times 10^{-5}$	$6.22 \times 10^2$	$1.62 \times 10^2$	$5.7 \times 10^3$	16.5

$$\begin{aligned}
g \frac{\partial}{\partial t} g_{oh}^R(\underline{v}, t) = & \frac{8\pi^2 e^2}{m^2} \sum_{n=-\infty}^{+\infty} \int d\underline{k} \frac{\mathcal{E}(\underline{k}, t)}{k^2} \left( \frac{n\Omega}{v_\perp} \frac{\partial}{\partial v_\perp} + k_\parallel \frac{\partial}{\partial v_\parallel} \right) \\
& \times [\delta(\omega_r - k_\parallel v_\parallel - n\Omega) J_n^2 \left( \frac{k_\perp v_\perp}{\Omega} \right) \left\{ \left( \frac{n\Omega}{v_\perp} \frac{\partial}{\partial v_\perp} + k_\parallel \frac{\partial}{\partial v_\parallel} \right) \right. \\
& \left. - \frac{n_0}{n_{oh}} \frac{v_h}{\Omega^2} k^2 \operatorname{Im}(N_h/D_h) \right\} g_{oh}^R] , \tag{28}
\end{aligned}$$

where the time evolution of the field energy density  $\mathcal{E}(\underline{k}, t)$  is given by

$$\frac{\partial}{\partial t} \mathcal{E}(\underline{k}, t) = 2 \operatorname{Im} \omega(\underline{k}, t) \mathcal{E}(\underline{k}, t) , \tag{29}$$

and  $N_h$  and  $D_h$  are given by Eqs. (14) and (15) with  $j=h$ , respectively, Equation (28) may be derived by following the standard method of the quasilinear theory. The superscript  $R$  on  $g_{oh}$  is to remind us that the equation is valid in the resonant region.

An H-theorem may be demonstrated from Eq. (28) by multiplying by  $g_{oh}^R$  and integrating over  $\underline{v}$ . This gives

$$\begin{aligned}
\frac{1}{2} \frac{d}{dt} \int d\underline{v} g_{oh}^{R2}(\underline{v}, t) = & - \frac{8\pi^2 e^2}{m^2} \sum_{n=-\infty}^{+\infty} \int d\underline{v} \int d\underline{k} \frac{\mathcal{E}(\underline{k}, t)}{k^2} \delta(\omega_r - k_\parallel v_\parallel - n\Omega) \\
& \times J_n^2 \left( \frac{k_\perp v_\perp}{\Omega} \right) \left\{ \left[ \left( \frac{n\Omega}{v_\perp} \frac{\partial}{\partial v_\perp} + k_\parallel \frac{\partial}{\partial v_\parallel} \right) g_{oh}^R \right]^2 \right. \\
& \left. - \frac{n_0}{n_{oh}} \frac{v_h}{\Omega^2} k^2 [\operatorname{Im}(N_h/D_h)] g_{oh}^R \left( \frac{n\Omega}{v_\perp} \frac{\partial}{\partial v_\perp} + k_\parallel \frac{\partial}{\partial v_\parallel} \right) g_{oh}^R \right\} . \tag{30}
\end{aligned}$$

Referring to Eqs. (14) and (15) we see that

$$\begin{aligned}
\operatorname{Im}(N_h/D_h) \approx & -\pi \frac{\Omega^2}{k^2} \frac{n_{oh}}{n_0} \sum_{n=-\infty}^{+\infty} \int d\underline{v} J_n^2 \left( \frac{k_\perp v_\perp}{\Omega} \right) \delta(\omega_r - k_\parallel v_\parallel - n\Omega) \\
& \times \left( \frac{n\Omega}{v_\perp} \frac{\partial}{\partial v_\perp} + k_\parallel \frac{\partial}{\partial v_\parallel} \right) g_{oh} . \tag{31}
\end{aligned}$$

Comparing the two terms inside the curly brackets on the right-hand side of Eq. (30) we conclude that the right-hand side of Eq. (30) is negative. Equation (30) then states that the time rate of change of a positive quantity is non-positive. Consequently, the time-asymptotic state must be the one for which the

integrand of the velocity integration on the right-hand side of Eq. (30) vanishes. That is,

$$\begin{aligned}
 \int_0^\infty \frac{dk_\perp}{k_\perp} \mathcal{E}(k_\perp, k_\parallel) &= \frac{\omega_r - n\Omega}{v_\parallel}, \quad t=\infty \quad \frac{J_n^2 \left( \frac{k_\perp v_\perp}{\Omega} \right)}{|v_\parallel|} \\
 &\times \left\{ \left[ \left( \frac{n\Omega}{v_\perp} \frac{\partial}{\partial v_\perp} + \frac{\omega_r - n\Omega}{v_\parallel} \frac{\partial}{\partial v_\parallel} \right) g_{oh}^R(v, \infty) \right]^2 - \frac{n_0}{n_{oh}} \frac{v_h}{\Omega^2} k_\perp^2 \operatorname{Im} \left[ \frac{N_h(\infty)}{D_h(\infty)} \right] g_{oh}^R(v, \infty) \right. \\
 &\left. \times \left( \frac{n\Omega}{v_\perp} \frac{\partial}{\partial v_\perp} + \frac{\omega_r - n\Omega}{v_\parallel} \frac{\partial}{\partial v_\parallel} \right) g_{oh}^R(v, \infty) \right\} = 0, \quad (32)
 \end{aligned}$$

where  $g_{oh}^R(v, \infty) = g_{oh}^R(v, t=\infty)$ , and  $N_h(\infty)$ ,  $D_h(\infty)$  are to be evaluated at  $k_\parallel = (\omega_r - n\Omega)/v_\parallel$ . It is expected that the field fluctuations will grow in time and then saturate at a finite amplitude level in the time-asymptotic state. In other words,  $\mathcal{E}(t=\infty) \neq 0$ . Then, according to Eq. (32),  $g_{oh}^R(v, \infty)$  is given by

$$\begin{aligned}
 &\left[ \left( \frac{n\Omega}{v_\perp} \frac{\partial}{\partial v_\perp} + \frac{\omega_r - n\Omega}{v_\parallel} \frac{\partial}{\partial v_\parallel} \right) g_{oh}^R(v, \infty) \right]^2 \\
 &= \frac{n_0}{n_{oh}} \frac{v_h}{\Omega^2} k_\perp^2 \operatorname{Im} \left( \frac{N_h}{D_h} \right) g_{oh}^R \left( \frac{n\Omega}{v_\perp} \frac{\partial}{\partial v_\perp} + \frac{\omega_r - n\Omega}{v_\parallel} \frac{\partial}{\partial v_\parallel} \right) g_{oh}^R. \quad (33)
 \end{aligned}$$

At this point we postulate that  $g_{oh}^R$  which is initially isotropic in velocity space remains so at all times. Then

$$\left( \frac{n\Omega}{v_\perp} \frac{\partial}{\partial v_\perp} + \frac{\omega_r - n\Omega}{v_\parallel} \frac{\partial}{\partial v_\parallel} \right) g_{oh}^R(v, \infty) = \frac{\omega_r}{v} \frac{\partial}{\partial v} g_{oh}^R(v, \infty) \quad (34)$$

where  $v = |\underline{v}|$ , and (33) becomes

$$\left[ \frac{\partial}{\partial v} g_{oh}^R(v, \infty) \right]^2 = \frac{n_0}{n_{oh}} \frac{v_h}{\Omega^2} \operatorname{Im} \left( \frac{N_h}{D_h} \right) \frac{k_\perp^2}{\omega_r} v g_{oh}^R \frac{\partial}{\partial v} g_{oh}^R. \quad (35)$$

Referring to Eq. (19), and using (34) we find

$$\operatorname{Im} \left[ \frac{N_h(\infty)}{D_h(\infty)} \right] = - \frac{2\Omega^2}{\omega_p^4} \omega_r \gamma(\infty) \quad (36)$$

where  $\gamma(\infty)$  is the time-asymptotic collisionless growth rate. Next, we assume that  $\gamma(\infty) = |\omega_c|$  so that the fluctuations do not grow any more. Here  $\omega_c$  is the collisional damping rate and may be taken as given by Eq. (18). Using this assumption in Eq. (35) we find

$$\left[ \frac{\partial}{\partial v} g_{\text{oh}}^R(v, \infty) \right]^2 = - \frac{n_0}{n_{\text{oh}}} \frac{v_m v_h}{\omega_p^4} k_\perp^2 v g_{\text{oh}}^R \frac{\partial}{\partial v} g_{\text{oh}}^R , \quad (37)$$

which can be solved to yield

$$g_{\text{oh}}^R(v, \infty) = C \exp(-\alpha v^2/2) ,$$

in the resonant region of the velocity space, where

$$\alpha = \frac{n_0}{n_{\text{oh}}} \frac{v_m v_h}{\omega_p^4} k_\perp^2 ,$$

and where the constant  $C$  has to be determined by matching this solution to the rest of the distribution function. Changing over to the energy representation we find

$$g_{\text{oh}}^R(E, \infty) \propto E^{1/2} \exp(-\alpha' E/E_0) , \quad (38)$$

where  $E_0$  is the peak energy of the suprathermal electrons and

$$\alpha' = \frac{1}{2} \frac{n_0}{n_{\text{oh}}} \left( \frac{v_m v_h}{\omega^2} \right) \left( \frac{\Omega}{\omega_p} \right)^4 K_\perp^2 , \quad (39)$$

with  $K_\perp \equiv k_\perp v_0 / \Omega$ . Using the values of the parameters involved,  $\alpha'$  is estimated to be  $\sim 10^{-2}$ . The expression (38) is valid for  $E > E_n$ , where  $E_n$  has been defined before, corresponding to the resonant region of the velocity space. We infer that in the resonant region the suprathermal electron distribution function, which initially had a positive slope, will have a small negative slope in the time-asymptotic state due to the wave-induced diffusion process. Of course, when the photoelectron source function, which is responsible for the bump in the equilibrium distribution function at  $t=0$ , is retained in the analysis the distribution function in the time-asymptotic state may have a small bump in the 2-6 eV region. For this a numerical analysis is required. Our conclusion is that the experimentally measured photoelectron distribution in the 2-6 eV energy range can be well explained if waves and wave-induced diffusion process are included in the theory of Jaspersel<sup>1</sup>.

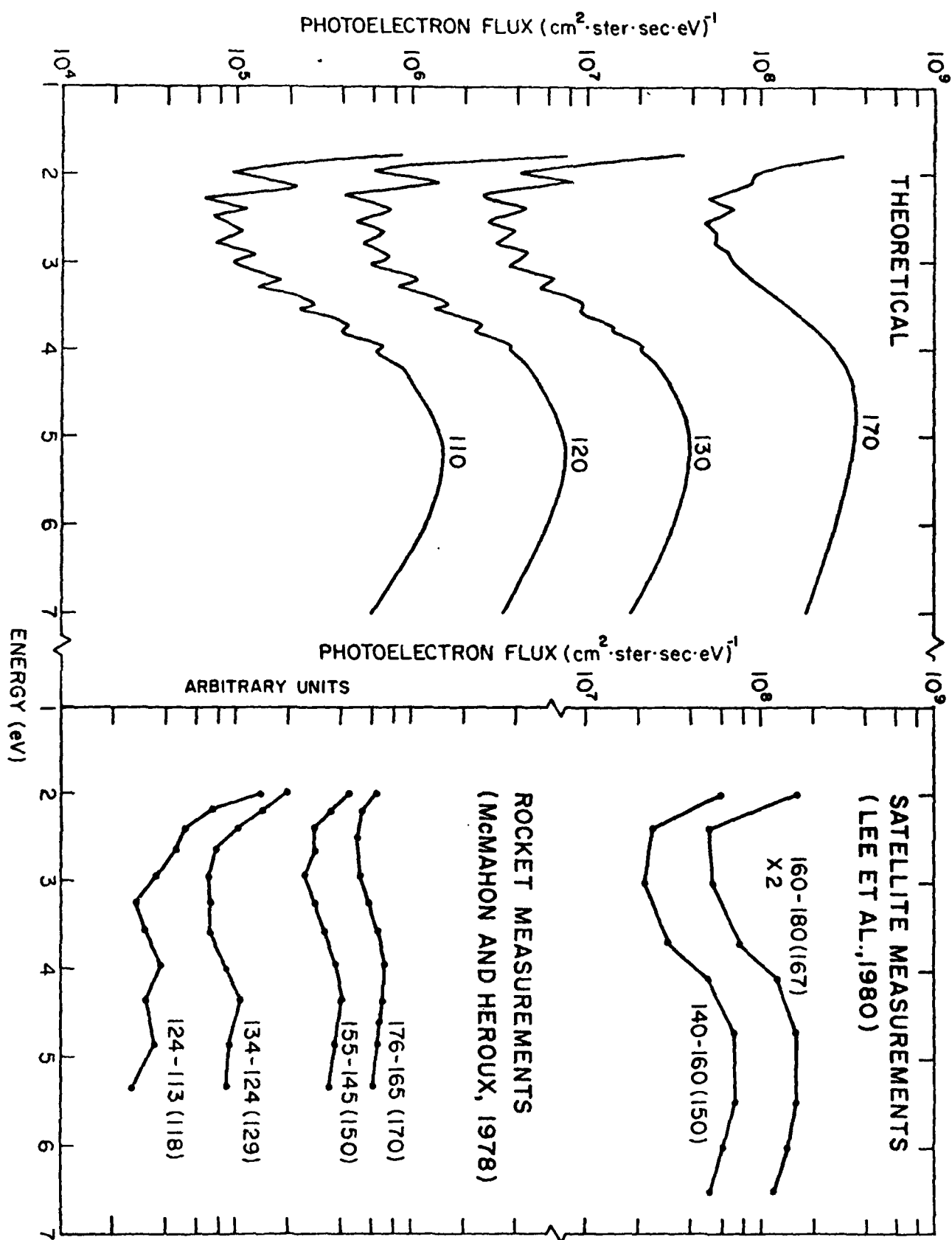


Figure I-1

## II. MODELING OF DAYTIME AIRGLOW AND ELECTRON DENSITY PROFILE IN THE MIDLATITUDE IONOSPHERE

Because of its influence on many Air Force communication and surveillance systems, it is of great importance to know the electron density profile (EDP) of the ionosphere. In circumstances where ionospheric sounders and other direct means cannot be used to determine this information, some means of modeling the EDP or determining it by remote sensing must be found.

One useful diagnostic of conditions within a plasma is the intensity of optical emission features at different wavelengths. In the daytime ionosphere, electrons released by photoionization excite atoms and molecules, which then emit photons at characteristic frequencies when they return to the ground state. Locally the emission rate depends on the density of the emitting species as well as the spectrum of the photoelectron flux. The overall emission measured along a line of sight will depend upon the profiles of these quantities.

In an effort to evaluate the practicality of using optical emissions as a remote sensor of the EDP, we have developed the capability of modeling the airglow emission of several features in the ultraviolet - the LBH bands and the spectral lines at 1356Å - emitted by the daytime, midlatitude ionosphere. For the daytime no method is yet known for determining the EDP directly from optical emissions; instead an indirect method, using optical emissions to constrain the parameters of a model of the EDP, will likely be necessary. In this report we describe a series of case studies, modeling the EDP using first-principle calculations and comparing the results to a variety of direct measurements. This series is aimed at evaluating how well such ab initio calculations can model the EDP and at determining which parameters of the model most sensitively control the EDP. For cases in which simultaneous optical emission measurements are available, we evaluate the emissions predicted by our model EDP and compare with the observed emissions.

In our ab initio calculations, the electron and ion densities are found by solving the continuity equations for all species simultaneously. In the bottom-side ionosphere transport can be ignored, and in the steady-state approximation the continuity equation for a species simplifies to a balance between its production and loss rates. The four most important ion species -  $O^+$ ,  $N_2^+$ ,  $O_2^+$ , and  $NO^+$  - are included in our model.

Above the EDP peak, the full time-dependent continuity equation including transport must be solved, although a simplification is achieved because only the dominant ion species,  $O^+$ , need be followed. We have modified an existing transport code so that it can run concurrently with our bottomside code. The result is a calculated EDP from 100 to 1000 km.

To calculate the intensity of VUV and UV daytime emissions, we begin with the photoelectron flux,  $F(E, z)$ , calculated as a function of energy and altitude. The volume emission rate at altitude  $z$  is given by

$$S_1(z) = n(z) \int F(E, z) \sigma(E) dE$$

where  $n(z)$  is the density of the emitting species and  $\sigma$  is the corresponding cross section. Integration of  $S_1(z)$  along the line of sight taking into account absorption gives us the column emmission rate.

The key parameters of these models are: 1) the solar EUV flux 2) the neutral atmosphere ( $N_2$ ,  $O_2$  and  $O$  densities), 3) the neutral wind and electric fields, and 4) the temperatures ( $T_e$ ,  $T_i$  and  $T_n$ ). Although the latter two are strictly parameters of the transport model for the EDP above the peak, the first two play a major role in determining the EDP throughout the daytime ionosphere.

It is unlikely that all the parameters needed to calculate an ab initio model of the EDP will be known in any particular case. To judge how much we could rely on estimates of unknown quantities, and how well our codes would perform, we conducted a series of tests under such circumstances, in which we could compare the results of our ab initio calculations directly with measured electron density profiles.

(1) Case One: White Sands Missile Range, August 23, 1972, Heroux  
et al., (1974).

This case involves rocket data for the solar EUV flux coincident with ground based ionosonde data. This represents a partial control on the production rate and should lead to good bottomside EDP agreement. In Figure II-1, we show a plot of the bottomside electron density profile from the ionosonde measurement and a graph of our hybrid calculation for the electron density profile. It should be noted that the estimated errors for the ionosonde measurement were  $\pm 30$  km near 120 km and  $\pm 5$  km elsewhere. For this case a Jacchia (1977) neutral atmosphere with the appropriate parameters for the given day was used in the calculation in addition to the measured solar EUV flux. Typical

daytime models were used for the electron temperature and neutral winds. With observational control on the solar flux one would expect good EDP agreement in and below the  $F_1$  layer. The agreement in the  $F_1$  layer is in fact within 15%, while the agreement in the E region is within the error bars on the ionosonde EDP. Unfortunately the unusually large error bar on the ionosonde measurement near 120 km renders the E region agreement of limited quantitative significance. The 25 km or 30% difference in the  $F_2$  peak of the EDP is consistent with any other state-of-the-art ab initio model calculation, and merely reinforces our intent to pursue the study of the transport term which is in all likelihood the source of this difference.

(2) Case Two: White Sands Missile Range, August 14, 1979

Rocket data for the solar EUV flux coincident with ground-based ionosonde data were again available for this case. Thus, we could use the measured solar flux, along with the appropriate Jacchia atmosphere model and the neutral wind and temperature models used in the previous case to calculate the ab initio model. The results, shown in Figure II-2, are similar to those of the previous case, although the accuracy of our calculated peak altitude happens to be better in this case, with the altitude of the calculated peak falling within 5 km of the measured position.

(3) Case Three: ISIS 2 topside sounder, May 23, 1972

The data considered here come from an ISIS 2 pass at 8:28 UT at  $60^\circ$  north latitude and  $38^\circ$  east longitude. The data were taken from iso-density contours in a sample collection of ISIS-2 observations (Klumpar, 1980). Due to reported difficulties in interpretation of sounder data, we have shown the data with  $\pm 50$  km error bars. Figure II-3 shows two theoretical curves with the topside sounder data. The solid curve shows the calculated profile using our best a priori estimates for the input quantities. We can see that the ab initio calculated profile is 60% lower than the data but agrees in shape. The dotted curve is a scaled version of the calculated profile fitted to the data. Had this been a nighttime case, we would expect direct VUV emissions as discussed in the next section to provide a good estimate of the peak of the EDP, to which the calculated topside EDP shape would then be scaled. This would lead to quite satisfactory agreement for this case. For the daytime case, the dashed curve would be essentially duplicated above 350 km by use of a stronger equatorward wind in

the model (as might follow at these latitudes from a high latitude heating event). The excellent agreement of the shape of the model and observed EDP satisfies necessary conditions for the merit of this EDP scheme. However, some additional observable must be added to scale the ab initio calculated EDP before we can look for the good agreement shown by the dashed curve.

(4) Case Four: Millstone Hill, incoherent scatter radar, April 8, 1978

This is another case in which the solar EUV flux and other input parameters for our model are unknown and we must attempt to estimate them. Using typical values for these parameters we calculated the EDP. Figure II-4 shows a comparison with the EDP derived from an incoherent scatter measurement. In this case the predicted peak is around 50 km above the measured peak, and densities can be as much as a factor of three in error.

Our conclusion from these four cases is that when we can specify the input data necessary for our EDP model, the model does well in fitting the actual EDP. When all the necessary data is not available, our model does a poorer job.

We now turn to cases in which optical emission data are available.

(5) Case Five: S3-4, Rev 373, April 8, 1978

In this case we had detailed optical emission data from a nadir-looking VUV spectrometer flying onboard DoD satellite S3-4,<sup>2</sup> but no simultaneous solar EUV flux or EDP measurements. To calculate airglow emission intensities we need, in addition to the parameters of our EDP model, the cross sections for the radiation processes. Because of the difficulty of laboratory measurements, some cross sections are still not well known. In Figure II-5 we show airglow calculations from our ab initio model for features at nine wavelengths, along with comparisons with the S3-4 data. We see that agreement is good at low wavelengths, around the feature at 1356Å, but that the agreement noticeably worsens at longer wavelengths where scattered light may be contaminating the data. The large error bars on the data points are due to the statistical uncertainty resulting from the low count rates in the data.

In Figure II-6 we track the optical emissions at 1356Å as the satellite moves along its orbit in the noon-midnight plane, passing through midday in the northern hemisphere. We find that our completely ab initio calculation does a remarkable job in reproducing the observed emissions produced under a wide range

of conditions. A similar plot for the feature at 1383Å (Figure II-7), shows our theory consistently low compared to the data.

#### (6) Case Six: Hilat Satellite July 1983

In this case we attempted to model the 1356Å airglow observed from the Hilat satellite. On the date of the observations the satellite passed overhead near a ground based ionosonde at Millstone Hill making near-coincident measurements of the EDP available.

The optical-emission measurements were made by the AIM sensor onboard Hilat at 22 hr 15 min 10 sec UT on Rev. 219. At that time, while crossing the latitude of Millstone Hill, the satellite passed 16.4° east of Millstone Hill. The AIM sensor scans through 135° along a path perpendicular to the satellite orbit, in this case beginning its sweep looking east into darkness and ending looking west into the bright limb, Figure II-8. There is some uncertainty in the orientation of the satellite, because in this rev. it was still oscillating on all three axes with the amplitude of the oscillation unknown. If we assume that the sensor was pointed in the nadir direction at the midpoint of the sweep, then the observed direction of the bright limb is displaced by one data bin, 5.64°, from its expected location. We assume that this gives us an estimate of the satellite roll, and we assign error bars of this magnitude to the directions of the calculated optical emissions. The look direction from the satellite to Millstone Hill is 53.62°W, placing Millstone Hill in the foot of the bright limb. An uncertainty of 5.6° in the look direction towards Millstone forces an uncertainty in the 1356Å flux of the order of 25%.

Our modeling began with a nadir calculation at the satellite location, with a solar zenith angle (SZA) of 81°. At this high SZA, the plane parallel approximation for the solar flux transport breaks down, resulting in an underestimation of the airglow emission rates. To get an upper bound for the airglow, a second nadir calculation was performed using an artificial value of the SZA, the angle whose secant approximates the Chapman function at 81°, that is, 79°. The results of the two calculations are plotted in Figure II-9 at pixel 160 (different pixels, are different look directions) we find that they are, respectively, 1.2 and 1.5 times the observed 1356Å airglow intensity in that direction.

To calculate the column emission rate at some angle to nadir a plane parallel approximation for the atmosphere was used. Calculations at 10, 20, 30, 40 and 53.62° (the look direction to Millstone Hill) are presented in Figure II-9. We see that the calculated emission profile reflects the profile of the data. At 53.62°, however, the change in SZA along the look direction was large enough to call the plane-parallel approximation into question. At that point we performed two airglow calculations to give bounds to the emission. One was based on the volume emission rate below the satellite, which with its higher SZA gives a lower bound to the airglow. The other calculation, based on the volume emission rate above Millstone, gives an upper bound. Figure II-9 shows the two results differing by a factor of two.

We were interested in this particular sweep because a ground-based ionosonde had measured the EDP just a half hour before the satellite fly-over. While not an ideal coincidence either spatially or temporally, this did give us an opportunity to compare our ab-initio calculations for the EDP and the airglow with observations of both quantities.

Comparison of the measured EDP with the ab initio EDP calculated for the airglow theory presented above shows that the ab initio EDP is consistently low (Figure II-10). We are currently working to find a method of adjusting the input parameters of our EDP calculation which can bring the calculated EDP into line with the measured EDP without destroying the fit of the calculated airglow emission to the observed airglow. One such adjusted model, shown in Figure II-10, was made by changing the neutral atmosphere to fit the model EDP to the measurements at the F2 peak. Such an adjustment, however, will also increase the already high optical emission rate.

The conclusion of this study then is that our ab initio calculations can perform fairly well when crucial input data can be accurately specified. Airglow measurements may be helpful in constraining parameters when the input data is inadequate. The future direction of this work should be aimed at establishing the correlations between the airglow and the EDP parameters so that the airglow measurements can be used for this purpose.

#### References

1. Heroux, L., M. Cohen, and J.E. Higgins, Electron Densities Between 110 and 300 km Derived From Solar EUV Fluxes of August 23, 1972, J. Geophys. Res., 79, 5237, 1974.
2. Huffman, R.E., F.J. Leblanc, J.C. Larrabee, and D.E. Paulsen, Satellite Vacuum Ultraviolet Airglow and Auroral Observations, J. Geophys. Res., 85, 2201, 1980.
3. Jacchia, L.G., Thermospheric Temperature, Density and Composition: New Models, Smithsonian Astrophysical Observatory Special Report 375, 1977.
4. Klumpar, D.M., ed., Coordinated Ionospheric and Magnetospheric Observations from the ISIS-2 Satellite by the ISIS-2 Experimenters, 3, (NSSDC/WDC-A-R+S,80) 1980.

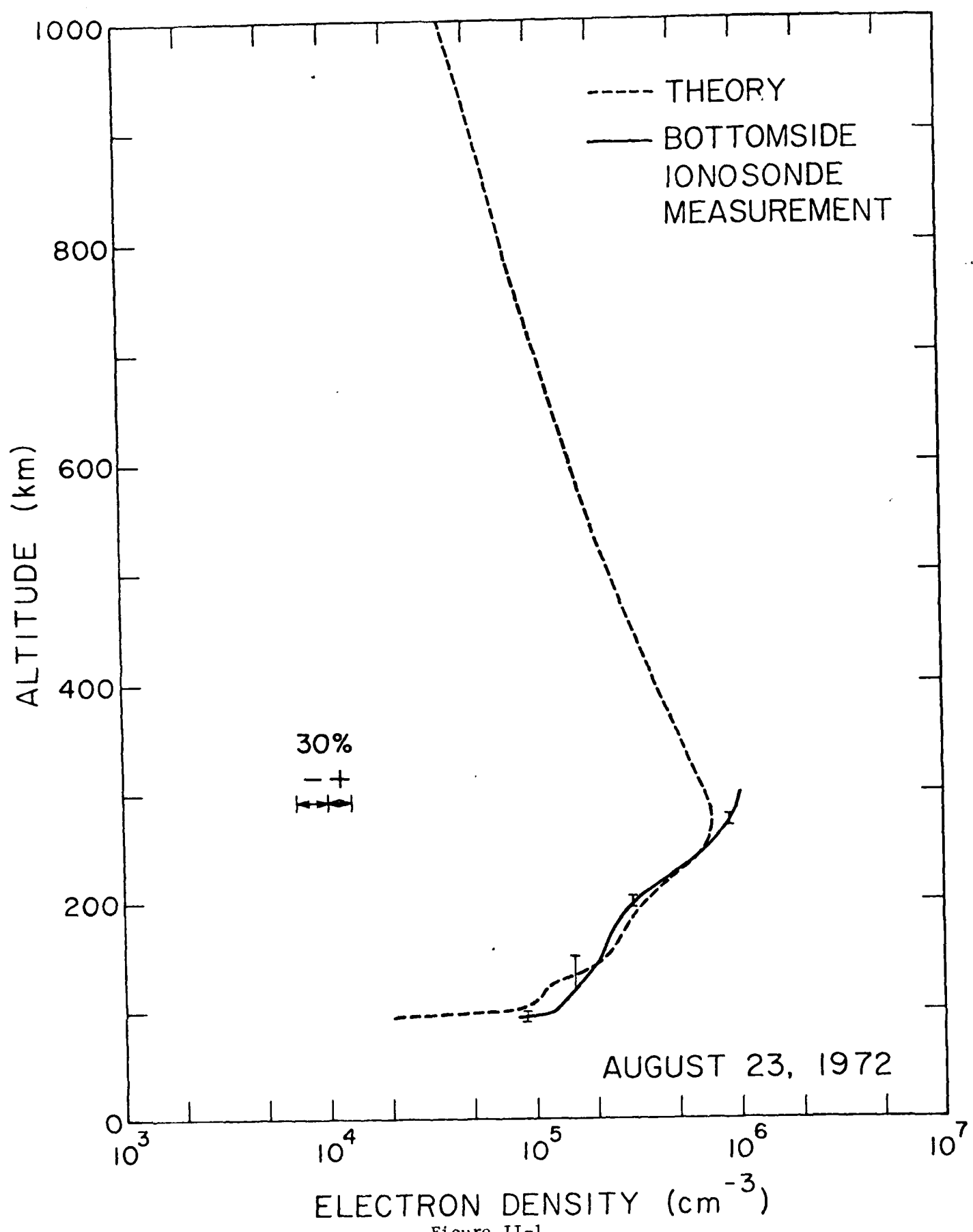
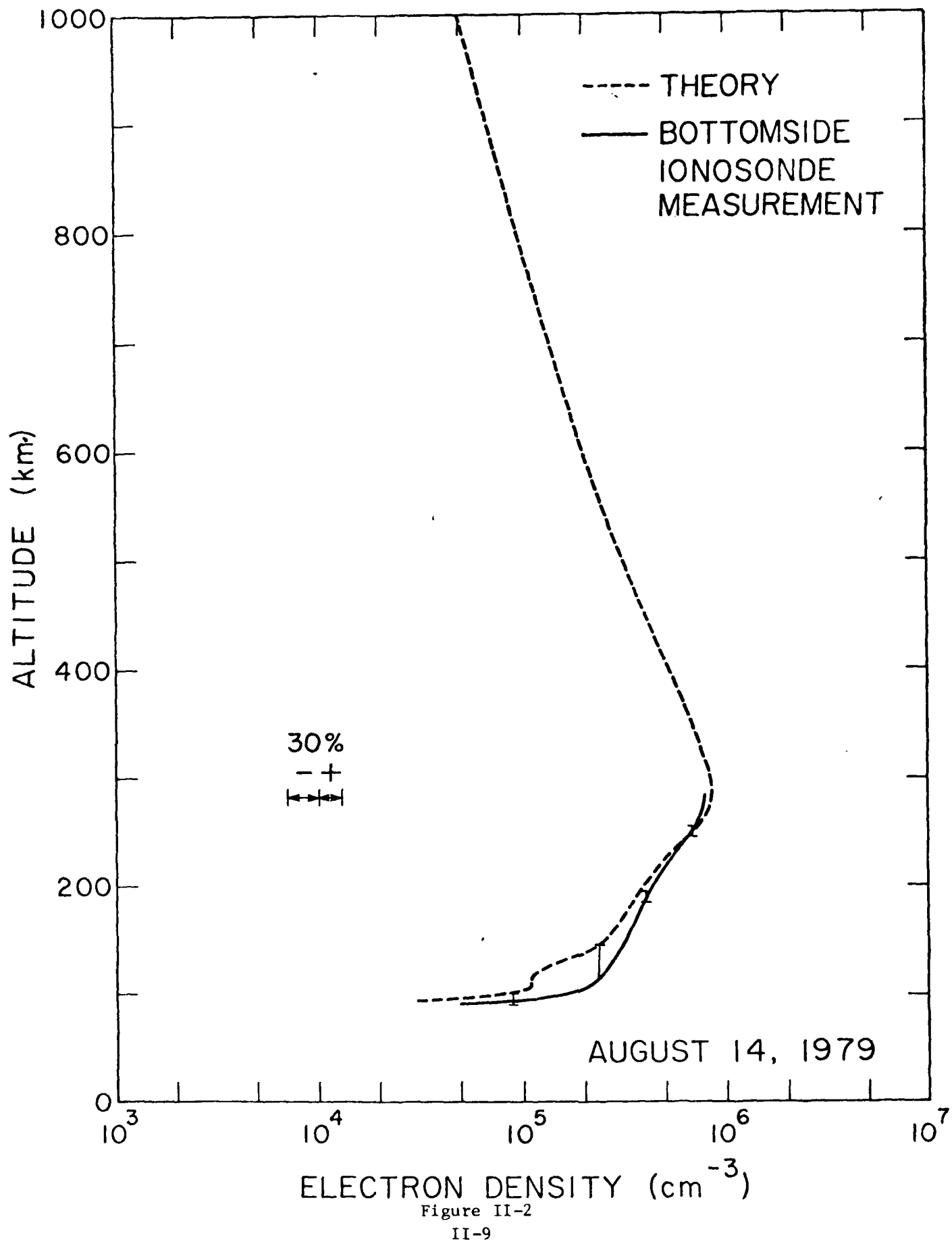
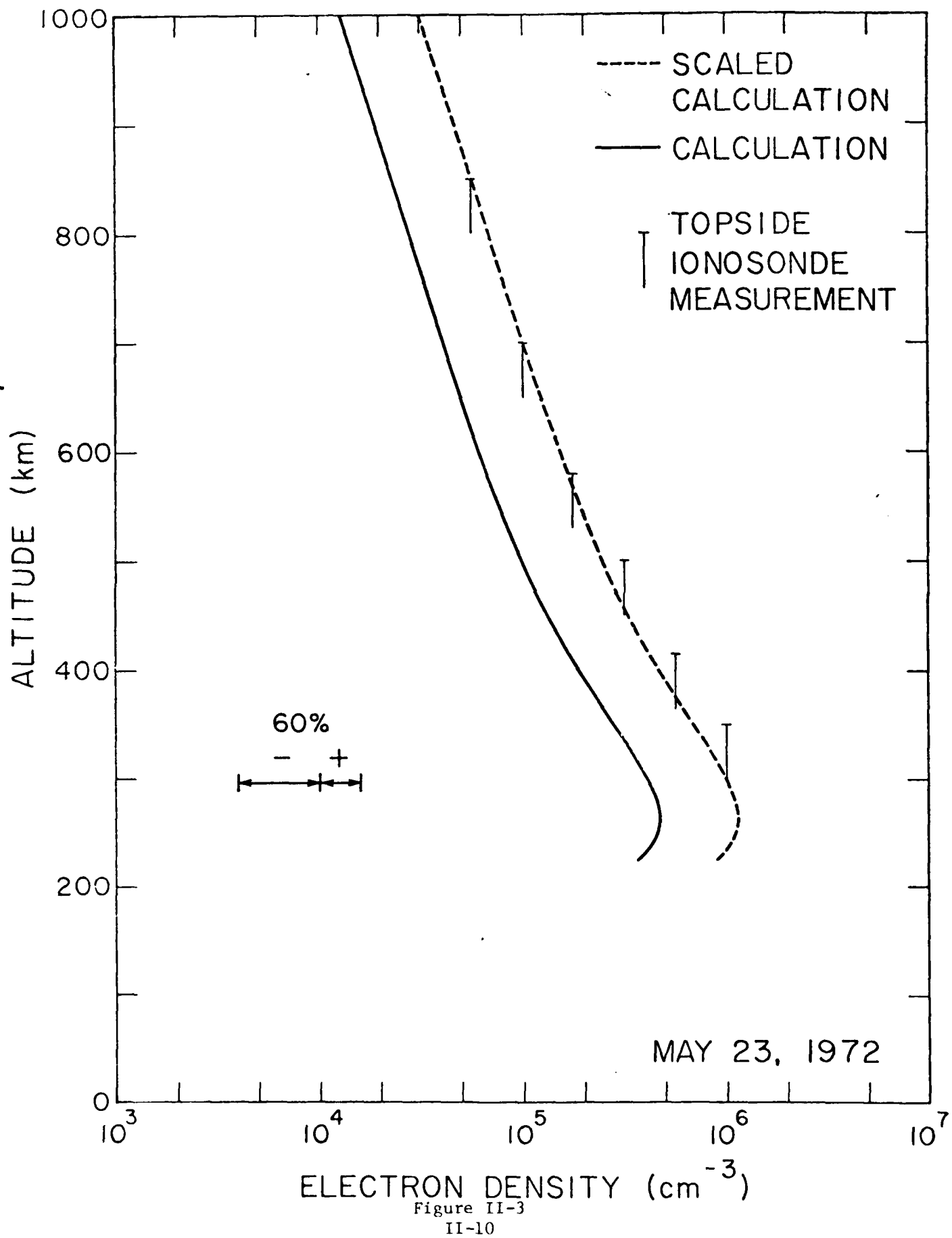


Figure II-1  
II-8





### INCOHERENT RADAR

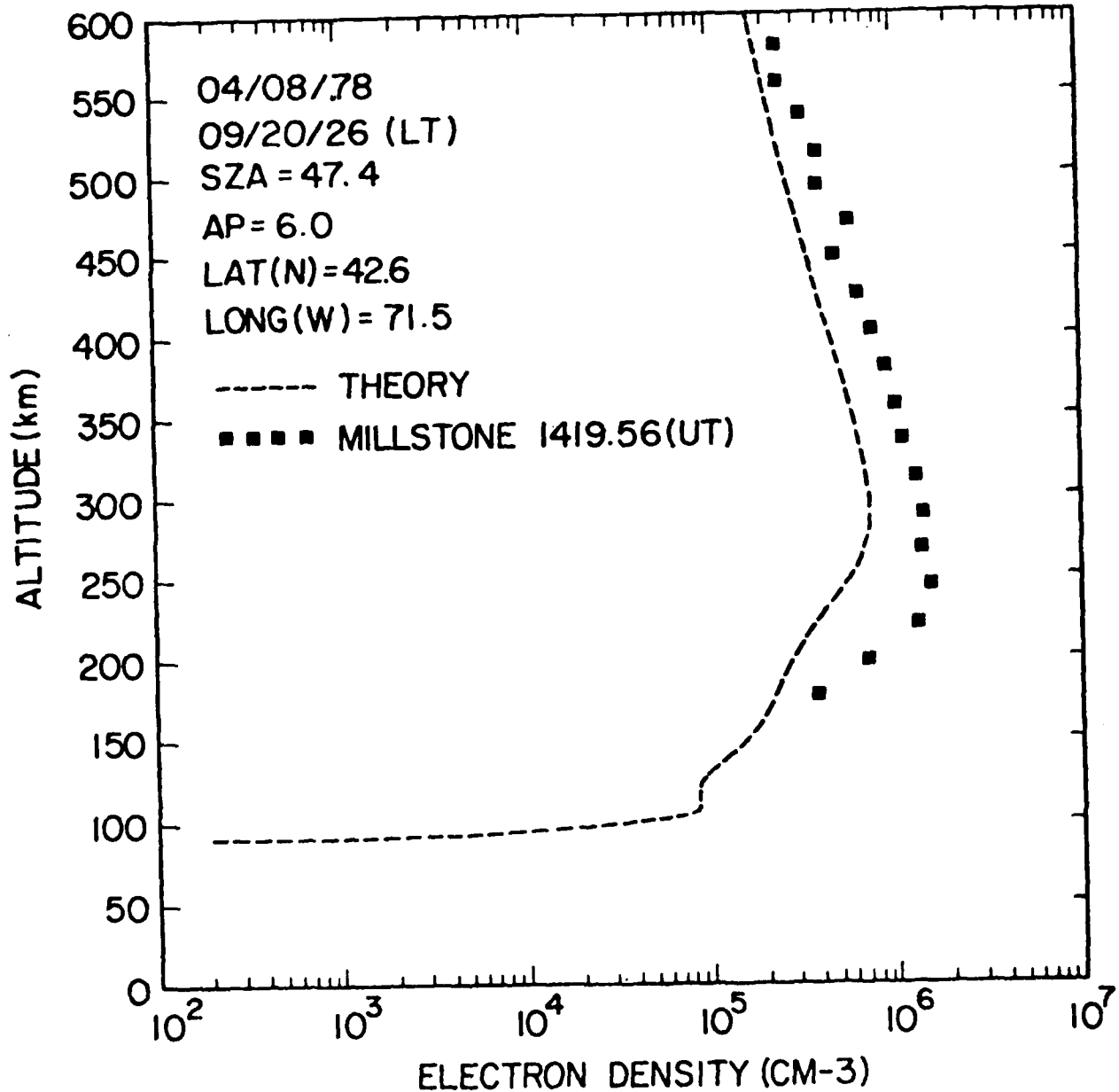


Figure II-4

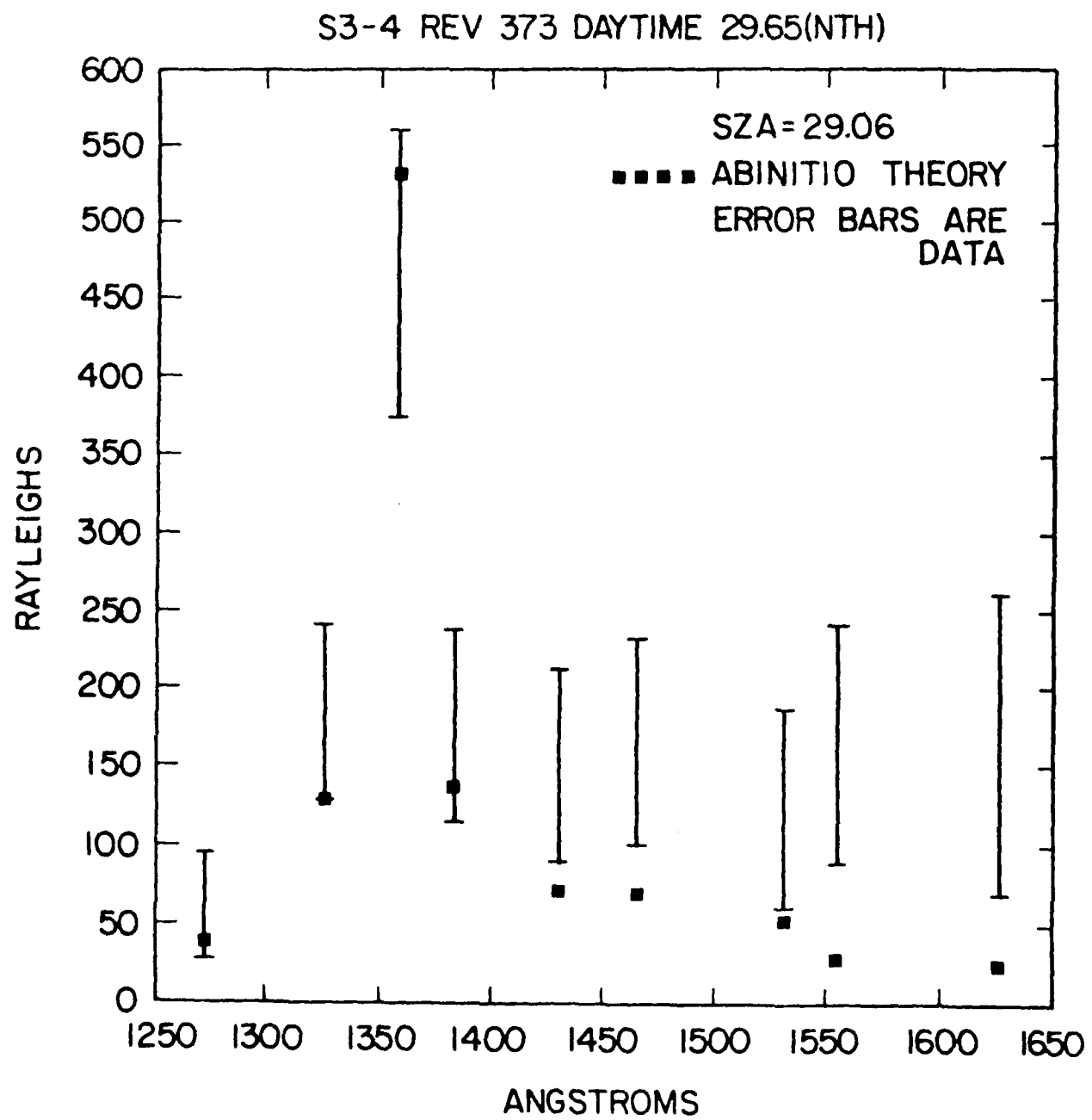


Figure II-5

S3-4 REV 373 DAYTIME 1356A

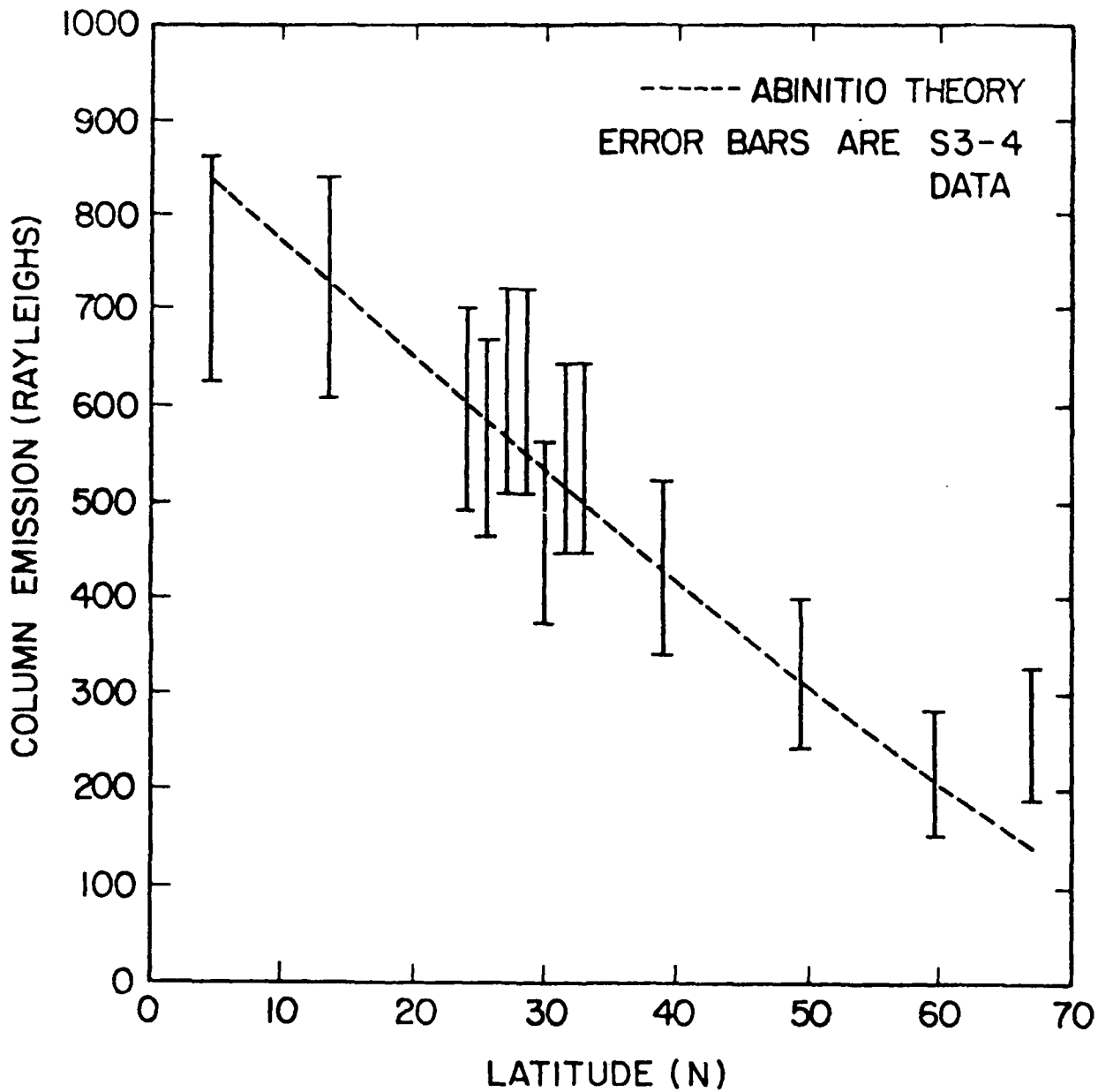


Figure II-6

S3-4 REV 373 DAYTIME 1383A

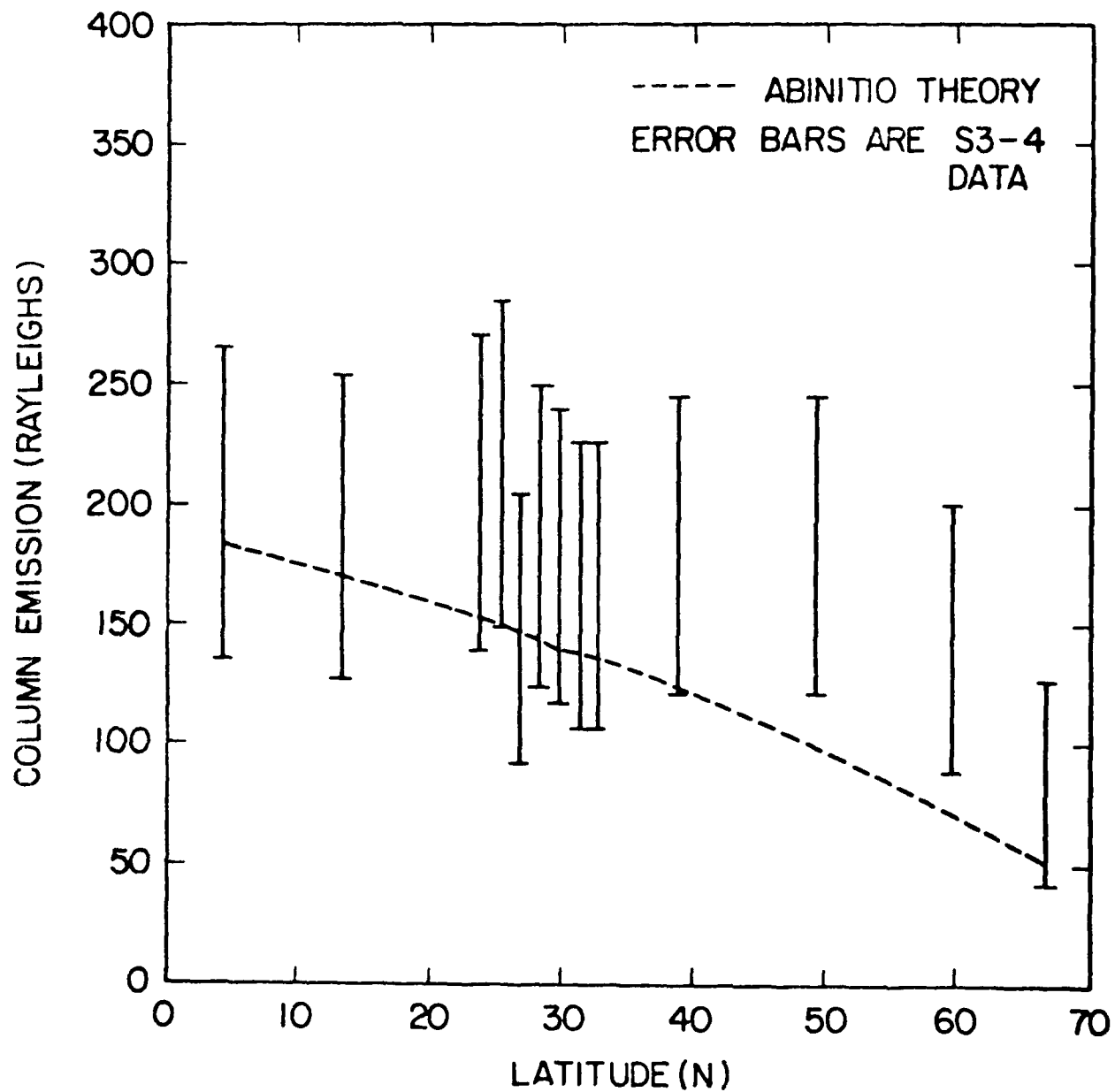
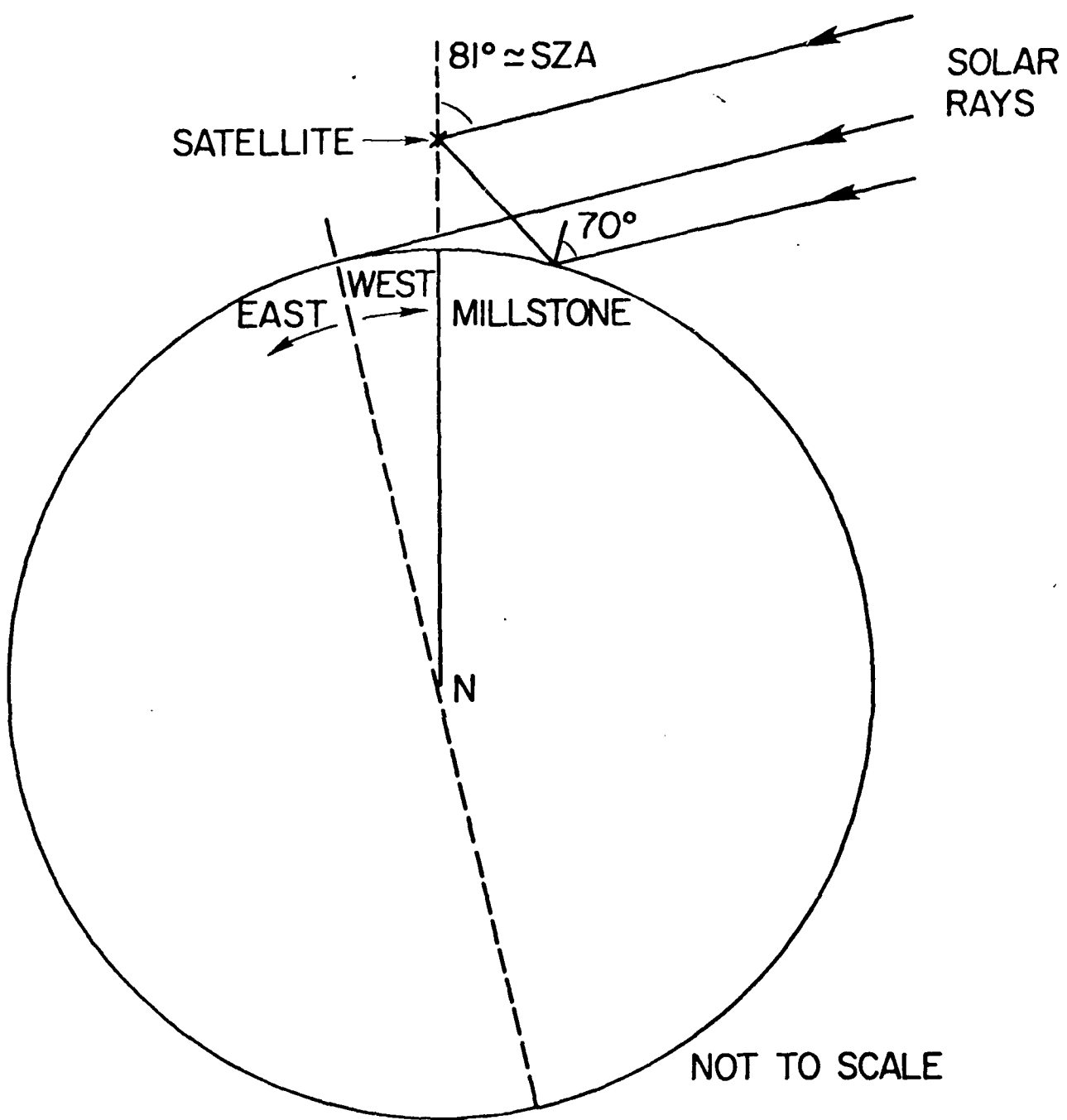


Figure II-7



RELATIVE POSITION OF HILAT, MILLSTONE  
AND THE SUN

Figure II-8

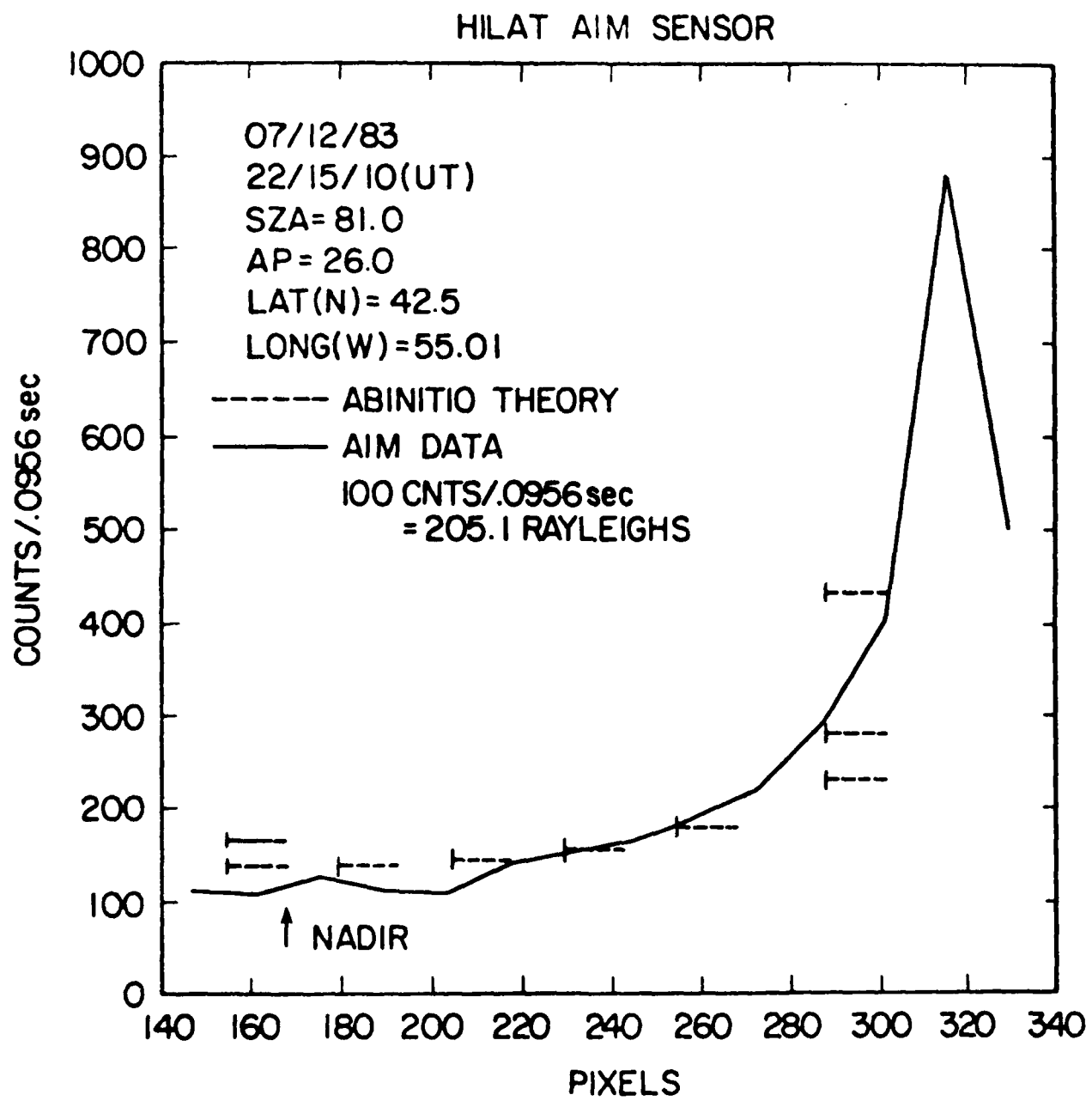


Figure II-9

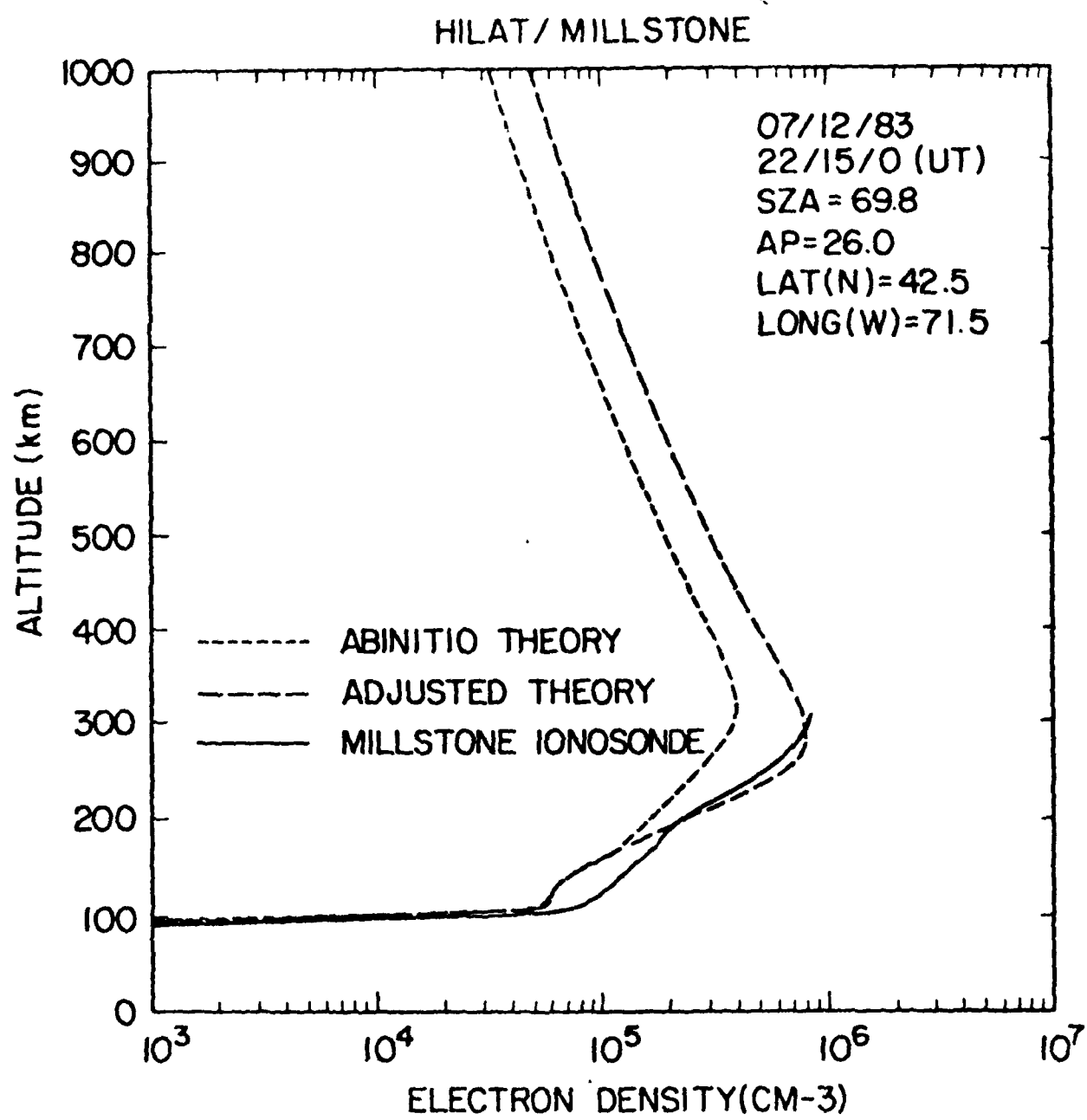


Figure II-10

### III. PARTICLE PRECIPITATION: MAGNETOSPHERE-IONOSPHERE COUPLING

The nighttime ionosphere at high latitudes, i.e., in the auroral zone, is created by energetic particles (both electrons and ions) precipitating from the magnetosphere. Calculations of energy deposition and ionization in the atmosphere<sup>1,2</sup> require that the incident flux of particles precipitating from the magnetosphere be specified. We have addressed this question with a study of the pitch angle diffusion process in the magnetosphere which causes particles to precipitate. The results of this study are summarized in subsection III.1, below. We were able to calculate the loss-cone population in the magnetosphere, as a function of position, when the processes of precipitation and diffusion compete against each other; the results are illustrated using data from the diffuse aurora.

In addition to ionization, the precipitating particles can also trigger plasma instabilities in the ionosphere, which can cause anomalous heating, irregularities, and other phenomena which interfere with communications. One of the sure indications of such activity in the aurora zone is the detection of ion conics: fluxes of energetic ions streaming out of the ionosphere along auroral field lines. We have studied both the means by which turbulence can be created by precipitating electrons and the way in which the turbulence can accelerate ionospheric ions. This work is summarized in subsection III.2, below. In an empirical study, using a Monte Carlo model for wave particle interaction, we were able to show that the commonly observed intense lower-hybrid turbulence in the supraauroral region is capable of accelerating ions to the energies commonly observed in ion conics. Then, using a plasma simulation, we demonstrated that a precipitating electron flux modeled after the flux observed in a discrete auroral arc could excite lower-hybrid turbulence and cause significant ion acceleration.

### III.1. The Loss-Cone Population in the Magnetosphere

Pitch-angle scattering has long been recognized as one of the important consequences of wave-particle interaction in the magnetosphere<sup>3</sup>. Its action continuously replenishes the flux of particles in the loss cone in velocity space, which gain access to the dense atmosphere and precipitate out of the magnetosphere<sup>4</sup>. Indeed, for the continuous (diffuse) aurora a common approximation is to assume that scattering is strong enough to maintain an isotropic particle distribution in the face of such anisotropic particle loss<sup>4</sup>. Detailed satellite observations<sup>5</sup>, however, show that electrons at keV energies and above are often anisotropic. At the low altitude of the ISIS satellite, the upward flowing loss cone, containing the few electrons backscattered from the atmosphere, is always strongly depleted. It is more interesting to find that the downward flowing loss cone, containing precipitating electrons, often shows a moderate depletion, too. While pitch-angle scattering has attempted to fill in the strongly depleted loss cone created at the other footpoint, its job is still unfinished when the particles reach the end of the field line and precipitate.

The effect of pitch-angle scattering by wave-particle interaction can be described by the quasilinear diffusion equation

$$\frac{\partial f}{\partial t} + \underline{v} \cdot \frac{\partial f}{\partial \underline{r}} + \frac{q}{m} (\underline{E} + \underline{v} \times \underline{B}/c) \cdot \frac{\partial f}{\partial \underline{v}} = \frac{\partial}{\partial \underline{v}} \cdot [D \cdot \frac{\partial f}{\partial \underline{v}}] \quad (1)$$

In this equation,  $f$  is the distribution function,  $E$  and  $B$  are the static fields and  $D$  is the quasilinear velocity diffusion coefficient due to fluctuating fields. (In a self-consistent treatment  $E$  would be determined from the particle populations via Poisson's equation or the condition of quasineutrality<sup>6</sup> and the diffusion coefficient would be determined from the turbulence arising from the instability of features in the particle distributions<sup>7</sup>. For the sake of simplicity, we regard these fields as given, imposed on the particles.)

When the spatial variation of the distribution function is weak, a fruitful simplification of this equation can be made by averaging over the bounce motion of a particle<sup>8</sup>. The resulting bounce-averaged diffusion equation has seen wide application<sup>8-10</sup> in the magnetosphere.

Far outside the loss cone the bounce-averaged diffusion equation can be justified because the spatial gradients are small. Inside the loss cone, however, the bounce-averaging approximations fail. When particles are removed

from the loss cone, sharp gradients in the distribution function are created at its edge. These gradients magnify the diffusion term so that significant change in the distribution function can occur over a time short compared to a bounce period. This implies significant variation of the distribution function along the orbit, which the bounce-averaged equation cannot describe.

To calculate the spatially varying distribution function, we must return to the full equation (1). Numerical solutions of (1) for the distribution function over all velocity space have been calculated by Davidson<sup>11</sup>. But the narrowness of the loss cone may be turned to our advantage, for it implies that we need to solve the spatially dependent problem only for that small region of velocity space. A boundary-layer treatment along this line has been developed for the loss cone in a mirror machine plasma<sup>12</sup> and for the stellar distribution around a black hole<sup>13</sup>. Basically one solves Eq. (1) in a simplified form for the loss cone, taking advantage of the smallness of the velocity-space region over which the solution is to apply, and matches that solution to a solution of the bounce averaged equation which applies outside the loss cone. We will use this method to describe the spatially dependent distribution function in the loss cone for the geomagnetic field. We will then apply the results to interpret particle data from a satellite pass through the continuous aurora. Readers interested in more detail than is presented here are referred to Ritterer *et al.*<sup>14</sup>.

### III.1.1 The Boundary-Layer Equation

The kinetic equation (1) describes both the random changes in velocity due to scattering and the systematic changes with position due to the mean fields. A simplification of the equation results when a change is made to variables incorporating the systematic changes, *viz.* particle energy and magnetic moment, or the magnitude of the velocity,  $v_0$ , and the pitch angle,  $\alpha_0$ , of the particle when it crosses the equatorial plane. Assuming that all other velocity gradients will be smaller, we retain only the pitch-angle gradients in the diffusion term. We will look for a quasisteady state solution for  $f$ : after possible initial transients the only time variation we expect is the slow decay of the population as the result of precipitation through the loss cone. With these approximations, the kinetic equation becomes

$$v_{\parallel} \frac{\partial f}{\partial s} = \frac{1}{J \sin \alpha_0} \frac{\partial}{\partial \alpha_0} [J \sin \alpha_0 D_0 \frac{\partial f}{\partial \alpha_0}] \quad (2)$$

where  $J$  is the Jacobian for the transformation from local velocity  $v$  to equatorial velocity  $v_0$ , and  $D_0$  is the familiar equatorial-pitch-angle diffusion coefficient (with units of  $\text{sec}^{-1}$ ). We simplify the equation further by introducing a scattering depth  $\tau$ , normalized to run from 0 to 1 as  $s$  runs from one footpoint of the field line  $-s_m$ , to the other at  $+s_m$ :

$$\tau = \frac{2}{\lambda} \int_{-s_m}^s \frac{ds}{v_{\parallel}} D_0 \quad (3)$$

where

$$\lambda = 2 \int_{-s_m}^{s_m} \frac{ds}{v_{\parallel}} D_0 = T_b \langle D_0 \rangle_b \quad (4)$$

$T_b$  is the bounce period, and  $\langle D_0 \rangle_b$  is the bounce averaged diffusion coefficient. Introducing the pitch-angle variable  $u$

$$u = \sin^2 \alpha_0 / 2\lambda \quad (5)$$

and using the small-angle approximation  $\sin \alpha_0 \approx \alpha_0$ , we reduce the kinetic equation to its final form:

$$\frac{\partial f(u, \tau)}{\partial \tau} = \frac{\partial}{\partial u} [u \frac{\partial f}{\partial u}] \quad (6)$$

### III.1.2 The Pitch-Angle Distribution

We solved Eq. (6) with the appropriate boundary conditions to find the distribution function as a function of pitch angle ( $u$ ) and position ( $\tau$ ). The solution has two parameters. The first is  $u_{\ell}$ , the value of  $u$  at the edge of the loss cone

$$u_{\ell} = \sin^2 \alpha_{0\ell} / 2 T_b \langle D_0 \rangle_b \quad (7)$$

This determines the degree of anisotropy within the loss cone; the larger  $u_{\ell}$  is, the larger is the size of the loss cone compared to the mean angle through which a particle is scattered during a bounce period and thus the greater is the depletion within the loss cone. The second parameter is an arbitrary normalization factor, which is determined (when needed) by matching the boundary-layer solution to the bounce-averaged solution outside the loss cone.

Figure III-1 illustrates the pitch angle distribution of precipitating particles (at  $\tau=1$ ) as the strength of scattering (the parameter  $u_\ell$ ) is changed. We see our expectation of increasing anisotropy with increasing  $u_\ell$  borne out. The dashed lines in this Figure are plots of an asymptotic solution to Eq. (6), calculated in the limit that  $\partial f/\partial \tau$  goes to zero:

$$f_{\text{asymp}} = \ln(u/u_\ell) + A \quad (8)$$

where  $A$  is independent of  $u$ . We see that the asymptotic form fits well at pitch angles only a little outside the loss cone, implying that spatial derivatives are already small at that point.

The variation of the pitch-angle distribution along the field line is illustrated in Figure III-2. This shows the filling in of the loss cone, which starts nearly empty at one end of the field line ( $\tau=0$ ), as  $\tau$  increases and the opposite end of the field line is approached. We have assumed reflection symmetry about the equatorial plane, so that the point  $\tau=1/2$  corresponds to the equator. This allows us to construct the populations in both loss cones at one point in space, by putting back-to-back the two distributions calculated at complementary values of  $\tau$ :  $\tau$  and  $1-\tau$ . This has been done in the insert in Figure III-2, for the case  $\tau=3/4$ . This shows a nearly empty upflowing ( $v_{\parallel} < 0$ ) loss cone along with a fuller downflowing ( $v_{\parallel} > 0$ ) one, much like the observed pitch-angle distributions<sup>5</sup>. None of this structure could have been calculated using the earlier bounce-averaged theory.

### III.1.3 Anisotropy in the Continuous Aurora

In the theory as it is formulated, the diffusion coefficient remains a free parameter. If it were possible to specify the amount of turbulence as a function of position, frequency and wavenumber, it would be possible to calculate the diffusion coefficient using quasilinear theory<sup>15</sup>. In practice, such detailed information about the turbulence is never available. Instead we can turn the problem around: from the detailed observations of particle anisotropy, we can infer the diffusion coefficient, and obtain valuable information concerning the turbulence. This empirical method has seen wide use in the radiation belts starting with<sup>3</sup>. An application of the method to data from a post break-up aurora, coupled with quasilinear estimates of the diffusion coefficient, allowed Lyons<sup>15</sup> to identify the turbulence there to be the result of unstable electron cyclotron harmonic waves. We go on to apply the method to

particle observations in the continuous aurora from the ISIS-2 satellite, kindly provided by James Sharber (Florida Institute of Technology).

The technique is to take the pitch-angle distribution measured at one energy during one spin of the satellite and fit our theoretical pitch-angle distribution to it by adjusting the parameter  $u_\ell$ . The results of this fitting are illustrated in Figure III-3. This shows the ISIS-2 data at several energies, for one spin cycle at inv. lat.  $\Lambda = 68.6^\circ$ . We see that anisotropy is small at low energies,  $E < 1$  keV, but that it grows as particle energy increases. Using appropriate values of the loss cone opening angle and bounce period, we then determine  $\langle D \rangle_b$  from  $u_\ell$  using Eq. (7). The results for the pitch-angle diffusion coefficient are shown in Figure III-4. Here we plot  $\langle D \rangle_b$  at several energies as a function of inv. latitude across the continuous aurora. We find that  $\langle D \rangle_b$  falls with energy roughly as a power law,  $E^{-n}$ , with  $n$  between one-half and unity. At fixed energy, the diffusion coefficient peaks at inv. lat.  $\Lambda \approx 69.6^\circ$ , where the precipitating energy flux into the ionosphere is also largest<sup>5</sup>. Cyclotron emissions are also known to be correlated with fluxes of 1-10 keV electrons<sup>6</sup> in this way, suggesting that such waves may be responsible for the scattering<sup>7</sup>.

#### III.1.4 Discussion

We have demonstrated how the effect of particle loss out of a loss cone in velocity space is gradually smoothed out along the field line by pitch-angle scattering. Our technique was applied to determine the amount of scattering necessary to account for the observed anisotropy of electrons precipitating in the continuous aurora.

The diffusion of electrons by turbulent fields, such as we have described, is only one aspect of the auroral precipitation problem. Another side is the generation of the fields as the result of instability of features in the particle distribution<sup>7</sup>. Each approach should form part of a self-consistent description of the total system of both particles and waves - a challenging problem for future work.

### III.2. Ion Acceleration in the Suprauroral Region

It is becoming more widely accepted that the energetic ion conics<sup>17</sup> observed below shock structures in the suprauroral region are produced as the result of ion acceleration by the VLF turbulence observed there<sup>18</sup>. The turbulence is generated through the instability of the auroral electron distribution accelerated parallel to the geomagnetic field by the shock<sup>19</sup>. A model for the formation of ion conics in this way was proposed by Chang and Coppi<sup>20</sup>. Acceleration nearly perpendicular to the field line by VLF turbulence near the lower hybrid frequency is followed by the adiabatic folding of velocities as the ions mirror and travel up the geomagnetic field line, creating the conic velocity distribution. Detailed calculations of conics using a Monte Carlo technique to model the wave-particle interaction were carried out by Rettler et al<sup>21</sup>.

#### 1) A Monte Carlo Model for Ion Acceleration

In the lower suprauroral region the electron cyclotron frequency is generally larger than the electron plasma frequency. Such an electron-ion plasma can support lower hybrid waves<sup>22</sup> with frequencies near the ion plasma frequency. For these modes,  $\Omega_i \ll \omega_{LH} \ll \Omega_e$ ,  $k_{\parallel} \ll k_{\perp}$ , and  $v_{te}/\Omega_e \ll k^{-1} \ll v_{ti}/\Omega_i$ . It has been shown that these lower hybrid waves can be generated quite efficiently by the electron beams produced by field-aligned DC potential drops during magnetic substorms<sup>19,20,23</sup>. Because of the broadband nature of the turbulence<sup>17</sup>, we cannot use a theory of acceleration by a coherent wave<sup>24</sup>. Instead, we apply the quasi-linear diffusion formulation for wave-particle interaction. Because of the frequencies and wavelengths involved, we may, in a first approximation, use the unmagnetized expression for the diffusion coefficient for the ions, given for example by Eq. (10.23) of Ichimaru<sup>25</sup>. (The excitation of LH waves with the unmagnetized approximation dropped has been studied by Basu et al.<sup>26</sup>.) The dynamical picture is completed by including the effects of the geomagnetic field and the DC electric field, along with the quasi-linear term, in a kinetic equation for the slow evolution of the ions:

$$\frac{\partial f}{\partial t} + v_{\parallel} \frac{\partial f}{\partial s} + \frac{q}{m} (\underline{E} + \frac{v}{c} \times \underline{B}) \cdot \frac{\partial f}{\partial \underline{v}} = \frac{\partial}{\partial \underline{v}} \cdot [D \cdot \frac{\partial f}{\partial \underline{v}}]. \quad (9)$$

In this equation  $f$  is the ion distribution function,  $v_{\parallel}$  is the velocity along  $s$ , which is a coordinate denoting position along the field line, and  $\underline{E}$  and  $\underline{B}$  are

the static fields. (Drifts perpendicular to  $B$  are ignored.) The quasilinear diffusion coefficient  $D$  is

$$D = \left(\frac{q}{m}\right)^2 \int \frac{d\omega}{2\pi} \int \frac{d^3k}{(2\pi)^3} \frac{\underline{k} \cdot \underline{k}}{|\underline{k}|^2} S_E(k, \omega) \pi \delta(\omega - \underline{k} \cdot \underline{v}) \quad (10)$$

where  $S_E$  is the spectral energy density in the turbulence.

Because of the inherent importance of its spatial structure, the time-dependent solution of the kinetic equation for the ions would be fully a four-dimensional problem - too complicated to be solved by standard finite-difference techniques. Instead we adopt a particle simulation model, in which the stochastic effects of wave-particle interactions are described using a Monte Carlo technique. Because the number of accelerated ions is small, we treat them as 'test particles' in externally imposed fields, instead of calculating the fields self-consistently.

From an initial distribution in velocity and space, the calculation of the evolution of the distribution proceeds by following the motion of a large number of ions with time. Because we are interested in changes occurring on scales much larger than the size of a gyroorbit, we need not integrate the equations of motion in detail. Instead, we follow only the motion of the particle guiding centers along the field line. Between the velocity perturbations caused by interaction with the waves, it is assumed that the ions travel in the inhomogeneous geomagnetic and DC electric fields with constant energy and first adiabatic invariant.

The wave-particle interactions are taken into account in the following way. In each time step  $\Delta t$ , the velocity of each particle is perturbed by an increment  $\Delta \underline{v}$  chosen according to a probability distribution  $P_{\Delta t}(\Delta \underline{v})$ . In kinetic-theory terms, the resulting change in the distribution  $f$  is given by the Smoluchowski equation<sup>27</sup>

$$f(\underline{v}, t + \Delta t) = \int f(\underline{v} - \Delta \underline{v}, t) P_{\Delta t}(\Delta \underline{v}) d^3 \Delta \underline{v} . \quad (11)$$

To model the quasilinear diffusion process, one chooses  $P_{\Delta t}(\Delta \underline{v})$  to be a gaussian function with the following moments

$$\langle \Delta \underline{v} \rangle = \nabla_v \cdot \underline{D} \Delta t \text{ and } \langle \Delta \underline{v} \Delta \underline{v} \rangle = 2 \underline{D} \Delta t \quad (12)$$

where  $\underline{D}$  is the quasilinear diffusion tensor. With this choice, the Fokker-Planck expansion of Eq. (11) yields the quasilinear diffusion equation in the limit that  $\Delta t \rightarrow 0$ . In the calculation, the probability distribution  $P_{\Delta t}(\Delta y)$  is sampled using random numbers. Among many other applications, this Monte Carlo technique has been used to introduce collisions into plasma simulations<sup>28,29</sup>. We go on now to apply the technique to the ion conic problem.

### III.2.1 The Formation of Ion Conics

To study ion conics in the lower suprauroral region, we carry out a simulation using the following parameters. Over the altitude range from 1000 to 5000 km we follow the evolution of  $H^+$  and  $O^+$  ions, whose initial density distribution decreases with the second power of the altitude - an approximation to Maeda's<sup>30</sup> model of ionospheric density. Their initial velocity distribution is an isothermal Maxwellian distribution, with a temperature of 1 eV. As the simulation progresses, we allow a steady state to be established by replacing every particle which leaves the simulation by a particle picked at random from the primordial distribution. For these first calculations, we include no DC potential drops.

The last parameter we must specify is the diffusion coefficient. To evaluate the quasi-linear term, we need to know the spectral density,  $S_E$ , of the lower hybrid turbulence. A self-consistent calculation of  $S_E(k, \omega)$  is complicated by the difficulty of determining the saturation mechanism of the lower hybrid instability, whether it occurs by nonlinear evolution or simply by convection out of the beam. We can sidestep that problem by using the experimentally observed amplitudes of the lower hybrid waves, which can range up to 50 mV/m and beyond<sup>31</sup>. In order of magnitude we have, in the range of resonant velocities,

$$D_L \approx \left(\frac{q}{m_i}\right)^2 \frac{|E_w|^2}{u_{pi}} \quad (13)$$

where  $|E_w|$  is the observed amplitude of the wave. The resonant range extends from a few times the ion thermal velocity up to a velocity  $v_{i\max} \sim u_{be} (k_{\parallel}/k_{\perp})$   $v_{i\max LH} \sim u_{be} (m_e/m_i)^{1/2}$ , where  $u_{be}$  is the velocity of the electron beam. Thus ions should stay in resonance until they reach energies near the electron beam energy, 1-10 keV. Above the upper limit  $v_{i\max}$ ,  $D_L$  should behave asymptotically as  $v_{\perp}^{-3}$ . Unfortunately, lack of knowledge of the wavenumber spectrum of the

turbulence prevents us from specifying the velocity dependence of the diffusion coefficient in any more detail than as a constant within the resonance limits. In practice, we will find that saturation of the heating is not caused by the resonance limit but instead by convection out of the region containing the turbulence. We consider several cases for the altitudinal range of turbulence: from narrowly spread, over a few km, to widely spread, over a thousand km. The actual spatial distribution is poorly known, although evidence shows<sup>31</sup> that broadband lower hybrid turbulence will be found below the electrostatic shock region whenever electron beams are detected.

Let us consider the model with a narrow range of turbulence first. In this case the heating and folding processes work almost independently of each other. In the steady state we find that the resonant ions have been heated to a characteristic energy of 10-20 eV when the turbulence range is 10 km. Their pitch-angle distribution remains sharply collimated at all altitudes, as it folds from near 90° at 1000 km to about 150° at 5000 km.

In contrast, when diffusion occurs over a wide range of altitude, the resulting conic structures are more diffuse. The continued transverse heating destroys the collimation. Figure III-5 illustrates the ion conic formed in this case, with a scatter point plot of particle kinetic energies parallel and perpendicular to the magnetic field. The lower panel of the figure presents the particles in the altitude range from 1000 km to 2000 km - the LH acceleration region in the simulation; the upper panel gives the ion conic after it has left the acceleration region, using the particles from 2000 km to 3000 km. The accelerated ions create a hot tail on the ion energy distribution, as Figure III-6 shows. Because of the wide extent of the acceleration region, particles reach high energies - up to a few keV in this case. The increase in energy is not greater because the heating is self-limiting: as a particle gains energy, it moves out of the heating region more quickly. The broader conics calculated in this second model are much like the conics seen by S3-3<sup>17</sup>.

### III.2.3 Discussion

We have illustrated the process of conic formation through transverse heating by lower hybrid waves and propagation along the geomagnetic field. Although we explicitly considered only H<sup>+</sup> ions in the calculations presented here, other calculations show that O<sup>+</sup> ions can be heated to energies comparable

to those of  $H^+$ ; the number of resonant  $O^+$  ions in a hydrogen dominated plasma, however, will be small.

Focusing on the broadband nature of LH turbulence, we have here adopted the quasilinear description of the acceleration process. Other workers have considered stochastic heating in the presence of a single wave. In the lower supraauroral region, where turbulence is intense but broadband, it is clear that neither approach is completely satisfactory. What is needed is a theory of strong turbulence. Once the wave-particle interaction in such a theory can be described in a probabilistic way, it is amenable to the Monte Carlo treatment presented here.

Considerable uncertainty remains in the model, however because of the difficulty in estimating the rate of the wave-particle interaction process. Empirical estimates of the velocity diffusion tensor based on observed wave amplitudes suffer because the lack of wavenumber measurements prevents us from determining the phase velocities of the waves. We cannot rely on linear calculations to give us the wave spectrum either, because there appears to be a real difficulty in linearly exciting waves of small enough phase velocity so that the resonant portion of the ambient ion distribution can account for the observed number of particles in the conics. In addition, the self-consistent evolution of the wave spectrum has been ignored in previous work.

## 2) Plasma Simulation

To address these problems, a plasma simulation was performed to provide an independent, self-consistent means of studying the generation of the turbulence and the resulting ion acceleration. The supraauroral situation was modeled by allowing a weak ( $n_b/n_0 \approx 10^{-2}$ ), energetic ( $E_b = 1$  keV), warm electron beam traveling along the magnetic field to destabilize a cool electron-ion plasma ( $T_e = T_i = 1$  eV). We set the direction of propagation of the waves to be nearly perpendicular to the magnetic field, with  $\cos^2\theta_B = m_e/m_i$  to reflect the observed wave spectral peak near 1.5 times the lower hybrid resonance frequency. The velocity of the 1 keV electron beam projected onto the propagation direction is then about 32 times the initial ion thermal velocity. The phase velocities of waves excited by this beam will be far out on the tail of the ion velocity distribution, where few ions can resonantly interact with them.

Nevertheless, a finite fraction of the ions are significantly accelerated in the course of the simulation. We found that tails of energetic ions formed, emerging from both sides of the initial distribution at about three times the ion thermal velocity; some ions are accelerated to velocities comparable to those of the electron beam. In addition to the tails the core of the velocity distribution showed evidence of nonresonant heating. It can be fitted by a Maxwellian velocity distribution, in which changes in the fitted thermal velocity reflect the changes in the total wave energy. But the tails account for most of the energy transferred to the ions in the course of the instability: immediately following wave saturation, at  $t = 400 \omega_{LH}^{-1}$ , they already contain 3% of the ions and account for half of the ion energy.

The interpretation of these results is clear, because it follows from the extensive work devoted to the high-frequency analogue of the problem: electron tail formation in strong Langmuir turbulence<sup>32</sup>. The intense VLF waves linearly excited by the beam parametrically decay into lower phase velocity VLF waves by coupling through nonresonant quasimodes which are driven to finite amplitude in the turbulent state. These lower phase velocity VLF waves are then Landau damped by the plasma, accelerating the ions perpendicular to the magnetic field and the electrons (because of their restricted perpendicular mobility) parallel to the field.

Several calculations support this interpretation of our simulation. First an analysis of the nonlinear dispersion relation<sup>33</sup> for the coupling of two lower hybrid waves through nonresonant quasimodes was performed. Using the amplitude and other parameters of one of the linearly excited waves in our simulation as a pump wave, we calculated the phase velocities of the sideband waves excited by the three-wave coupling process. We found that these velocities agreed well with the velocities at the points where the tails emerge from the background distribution, supporting the argument that Landau damping of these sidebands accelerates the ions. Second, direct simulation of the parametric decay of a lower hybrid pump wave<sup>34</sup> was found to lead to perpendicular ion acceleration accompanied by parallel electron acceleration. Finally, we formulated a simple set of kinetic equations containing the quasilinear equations with mode coupling terms to describe the parametric processes. Numerical solution of these

equations produces ion velocity distribution with high energy tails and a wave spectrum similar to the ones observed in the simulation.

### III.2.3 Conclusion

Scaling of our simulation results to supraauroral conditions gives results which agree well with data from observed ion conics: fraction of accelerated ions  $\sim 10^{-3}$  to  $10^{-2}$ : average energy  $\sim 50$  eV: maximum energy  $\sim 1$  keV: observed lower hybrid wave amplitude ranging up to 50 mV/m. We conclude that the VLF turbulence generated below field aligned potential drops in the supraauroral region can account for the acceleration of ions observed in ion conic events.

## References

- 1) Jasperse, J.R. and Basu, B., Transport theoretic solutions for auroral proton and H atom fluxes and related quantities, J. Geophys. Res., 87, 811, 1982.
- 2) Strickland, D.J. et al., Transport equation techniques for the deposition of auroral electrons, J. Geophys. Res., 81, 2755, 1976.
- 3) Kennel, C.F. and Petschek, H., Limit on stably trapped particle fluxes, J. Geophys. Res., 71, 1, 1966.
- 4) Kennel, C.F., Consequences of a magnetospheric plasma, Rev. Geophys. Space and Sci., 7, 379, 1969.
- 5) Sharber, J.R., in "Physics of Space Plasmas", edited by Chang, T., Coppi, B., and Jasperse, J.R., The continuous (diffuse) aurora and auroral-E ionization (Scientific Publishers, Cambridge, MA, 1981).
- 6) Chiu, Y.T. and Schulz, M., Self-consistent particle and parallel electrostatic field distributions in the magnetospheric - ionospheric auroral region, J. Geophys. Res., 83, 629, 1978.
- 7) Kennel, C.F. and Ashour-Abdalla, M., Electrostatic waves and the strong diffusion of magnetospheric electrons, in "Magnetospheric Plasma Physics", edited by Nishida, A. (D. Reidel, Hingham, MA 1982).
- 8) Lyons, L.R., Thorne, R. and Kennel, C., Pitch-angle diffusion of radiation belt electrons within the plasmasphere, J. Geophys. Res., 77, 3455, 1972.
- 9) Lyons, L.R., Comments on pitch-angle diffusion in the radiation belts, J. Geophys. Res., 78, 6793, 1973.
- 10) Spjeldvik, W.N. and Thorne, R., The cause of storm aftereffects in the middle latitude D region, J. Atmos. Terr. Phys., 37, 777, 1975.
- 11) Davidson, G.T., Pitch angle diffusion of trapped particles in the presence of a loss cone: Calculating the distribution of particles precipitating from the earth's radiation belts, J. Comput. Phys., 31, 301, 1979.
- 12) Baldwin, D., Cordey, J. and Watson, C. Plasma distribution function near the loss cone of a mirror machine, Nuc. Fusion, 12, 307, 1972.
- 13) Cohn, H. and Kulsrud, R., The stellar distribution around a black hole: Numerical integration of the Fokker-Planck equation, Astrophys. J., 226, 1087, 1978.
- 14) Retterer, J.M., Jasperse J. and Chang, T., A new approach to pitch angle scattering in the magnetosphere, J. Geophys. Res., 88, 201, 1983.
- 15) Lyons, L.R., Electron diffusion driven by magnetospheric electrostatic waves, J. Geophys. Res., 79, 575, 1974.

- 16) Anderson, R.R. and Maeda, K., VLF emissions associated with enhanced magnetospheric electrons, J. Geophys. Res., 82, 135, 1977.
- 17) Mizera, P., et al., The aurora inferred from S3-3 particles and fields, J. Geophys. Res., 86, 2329, 1981.
- 18) Temerin, M., Plasma waves on auroral field lines, in Auroral Arcs, AGU Monograph 25 (AGU, Washington, 1981).
- 19) Maggs, J., Coherent generation of VLF hiss, J. Geophys. Res., 81, 1707, 1976.
- 20) Chang, T. and Coppi, B., Lower hybrid acceleration and ion evolution in the supraauroral region, Geophys. Res. Lett., 8, 1253, 1981.
- 21) Retterer, J.M., et al., Ion acceleration in the supraauroral region: A Monte Carlo model, Geophys. Res. Lett., 10, 583, 1983.
- 22) Coppi, B., Pegoraro, F., Pozzoli, R. and Rewoldt, G., Slide-away distribution and relevant collective modes in high temperature plasmas, Nuc. Fusion, 16, 309, 1976.
- 23) Papadopoulos, K. and Palmadesso, P., Excitation of lower hybrid waves in a plasma by electron beams, Phys. Fluids, 19, 605, 1976.
- 24) Lysak, R., Hudson M. and Temerin, M., Ion heating by strong electrostatic ion cyclotron turbulence, J. Geophys. Res., 85, 678, 1980.
- 25) Ichimaru, S., Basic Principles of Plasma Physics: A Statistical Approach, W.A. Benjamin, Reading, MA 1973.
- 26) Basu, B., Chang, T. and Coppi, B., Energization of ions by long wavelength lower hybrid waves, In Proceedings of 1982 International Conference on Plasma Physics, H. Wilhelmson and J. Weiland (ed.) 1982.
- 27) Chandrasekhar, S., Stochastic problems in physics and astronomy, Rev. Mod. Phys., 15, 1, 1943.
- 28) Shanny, R., Dawson J. and Greene, J., One dimensional model of a Lorentz plasma, Phys. Fluids, 10, 1281, 1967.
- 29) Spitzer, L. and Hart, M., Random gravitational encounters and the evolution of spherical systems, Astrophys. J., 164, 399, 1971.
- 30) Maeda, K., A Calculation of auroral hiss with improved models for geoplasma and magnetic field., Planet. Spa. Sci., 23, 843, 1975.
- 31) Temerin, M., et al., The small scale structure of electrostatic shocks, J. Geophys. Res., 86, 11, 278, 1981.
- 32) Kruer, W., Saturation and nonlinear effects of parametric instability, in Advances in Plasma Physics, Vol. 6 (Wiley, New York, 1967).

- 33) Porkolab, M., Parametric instabilities due to lower hybrid radio frequency heating of tokamak plasmas, Phys. Fluids, 20, 2058, 1977.
- 34) Chu, C., Dawson, J.M. and Okua, H., Plasma heating at frequencies near the lower hybrid, Phys. Fluids, 19, 981, 1976.

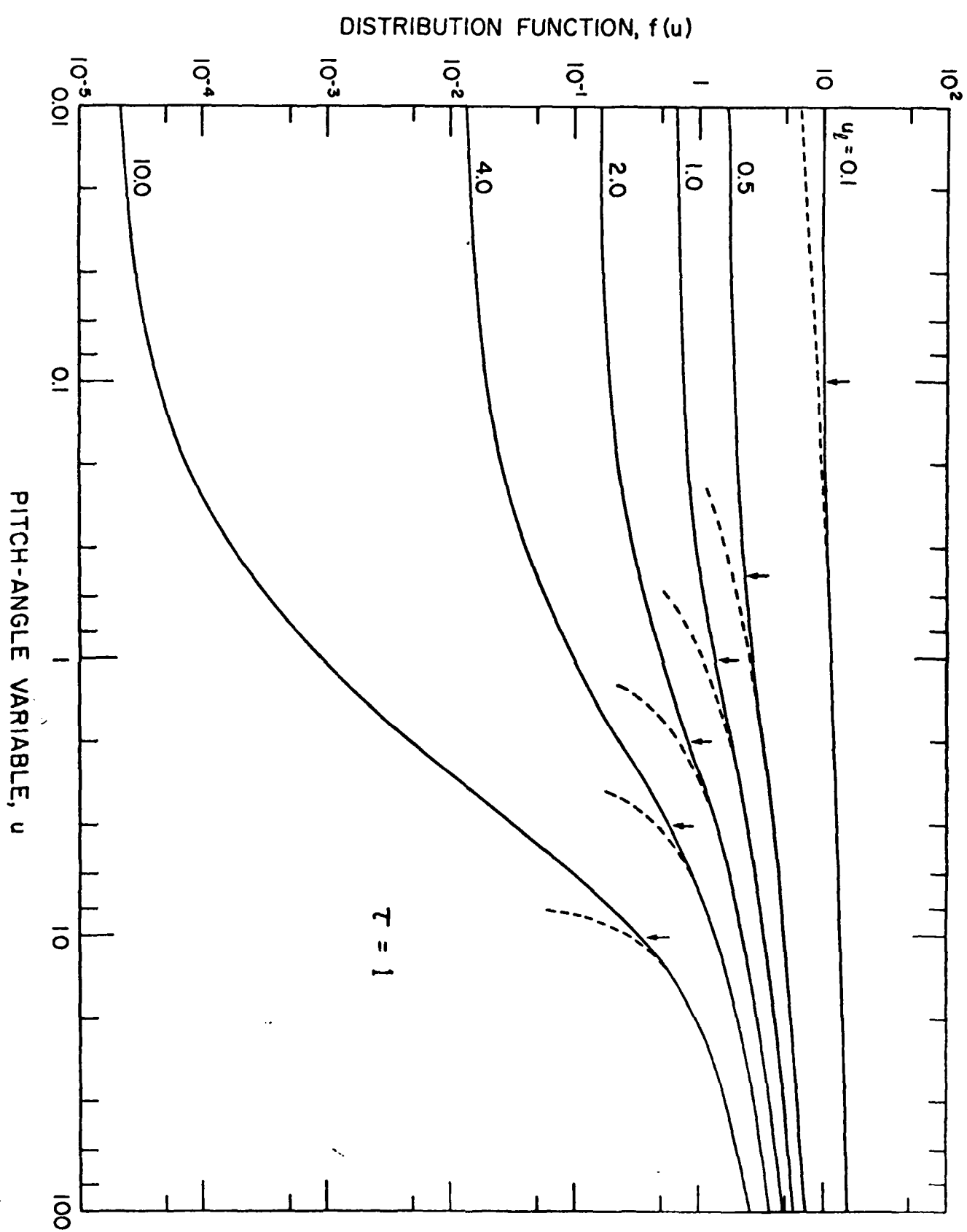


Figure III-1

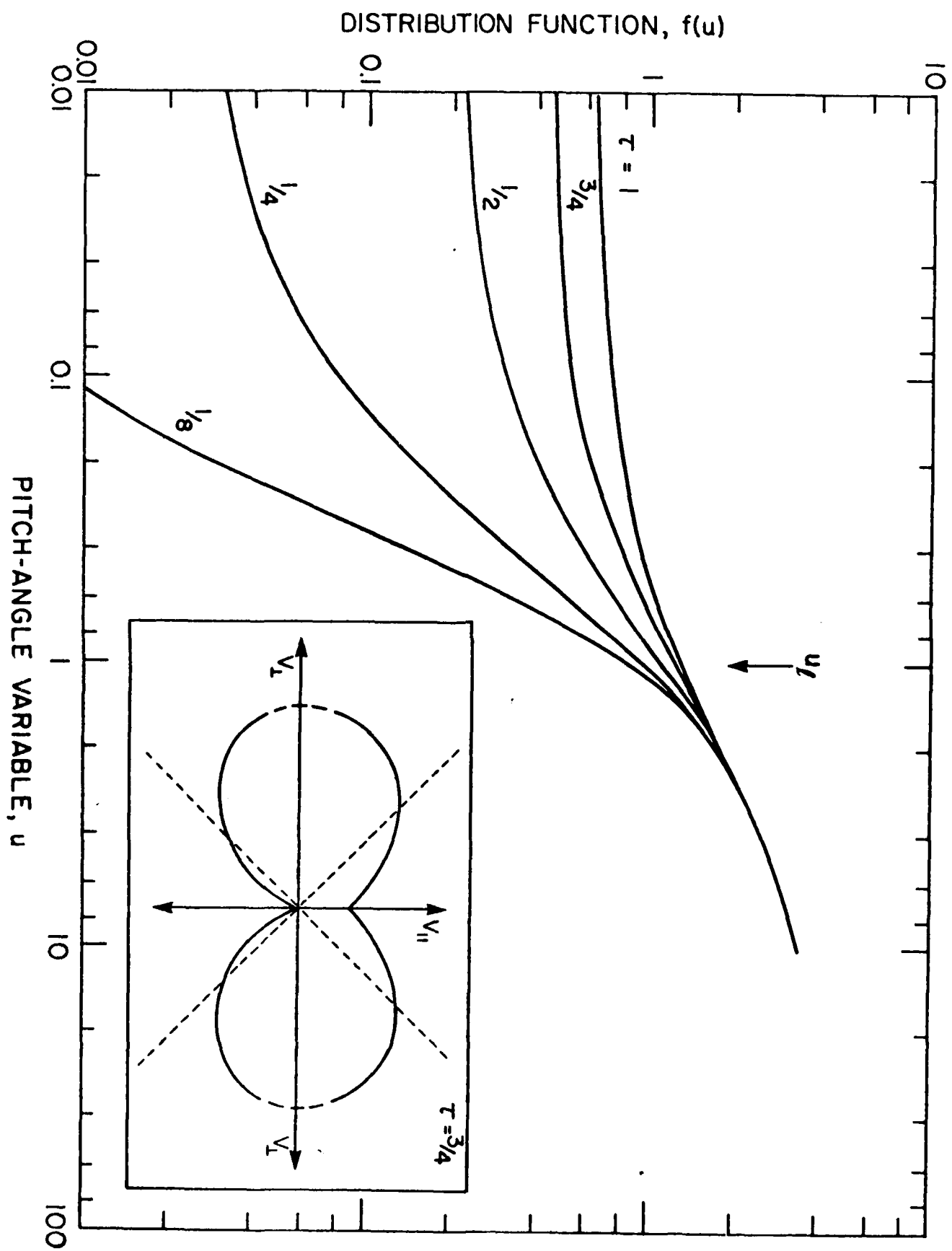


Figure III-2

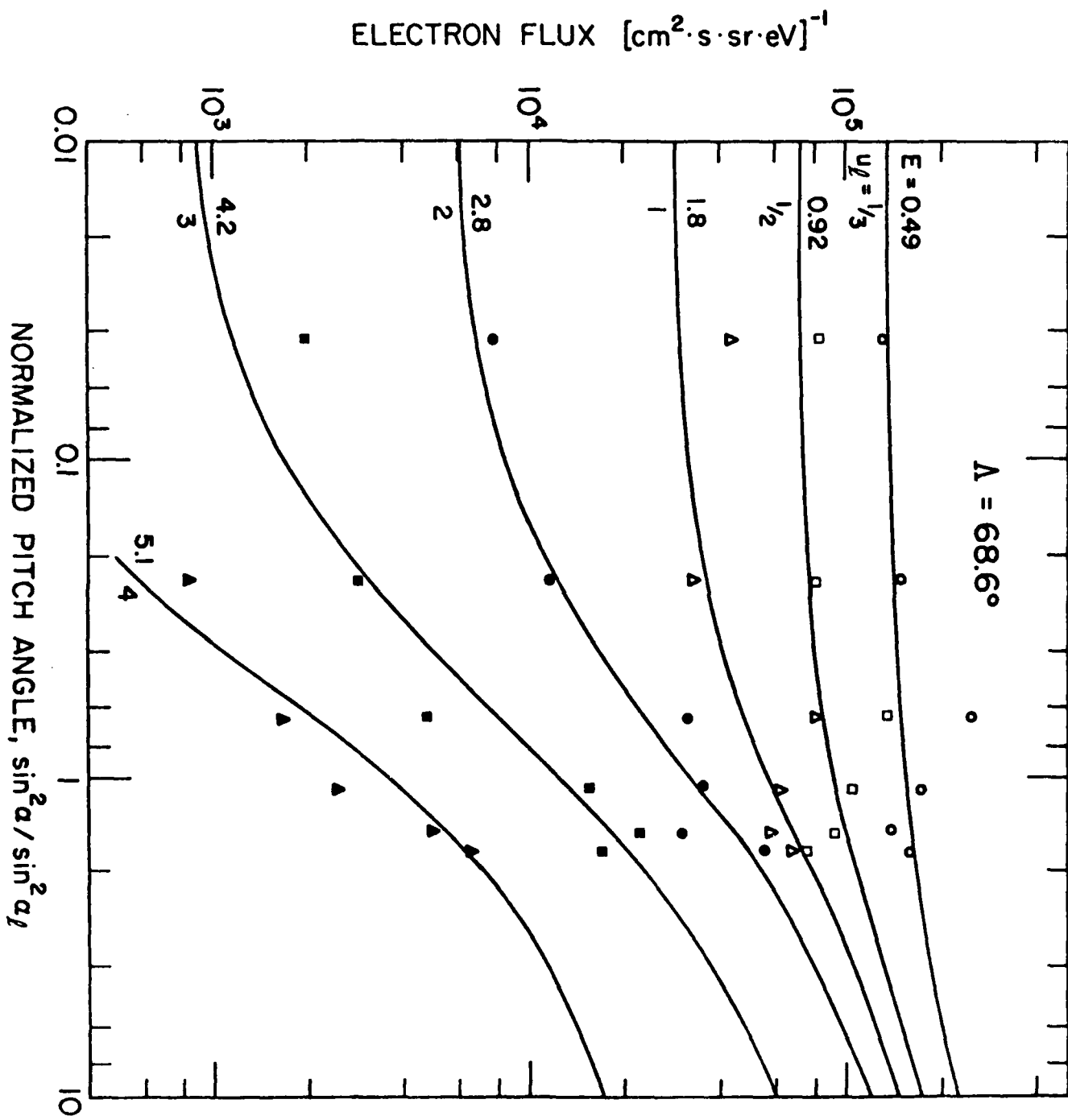


Figure III-3

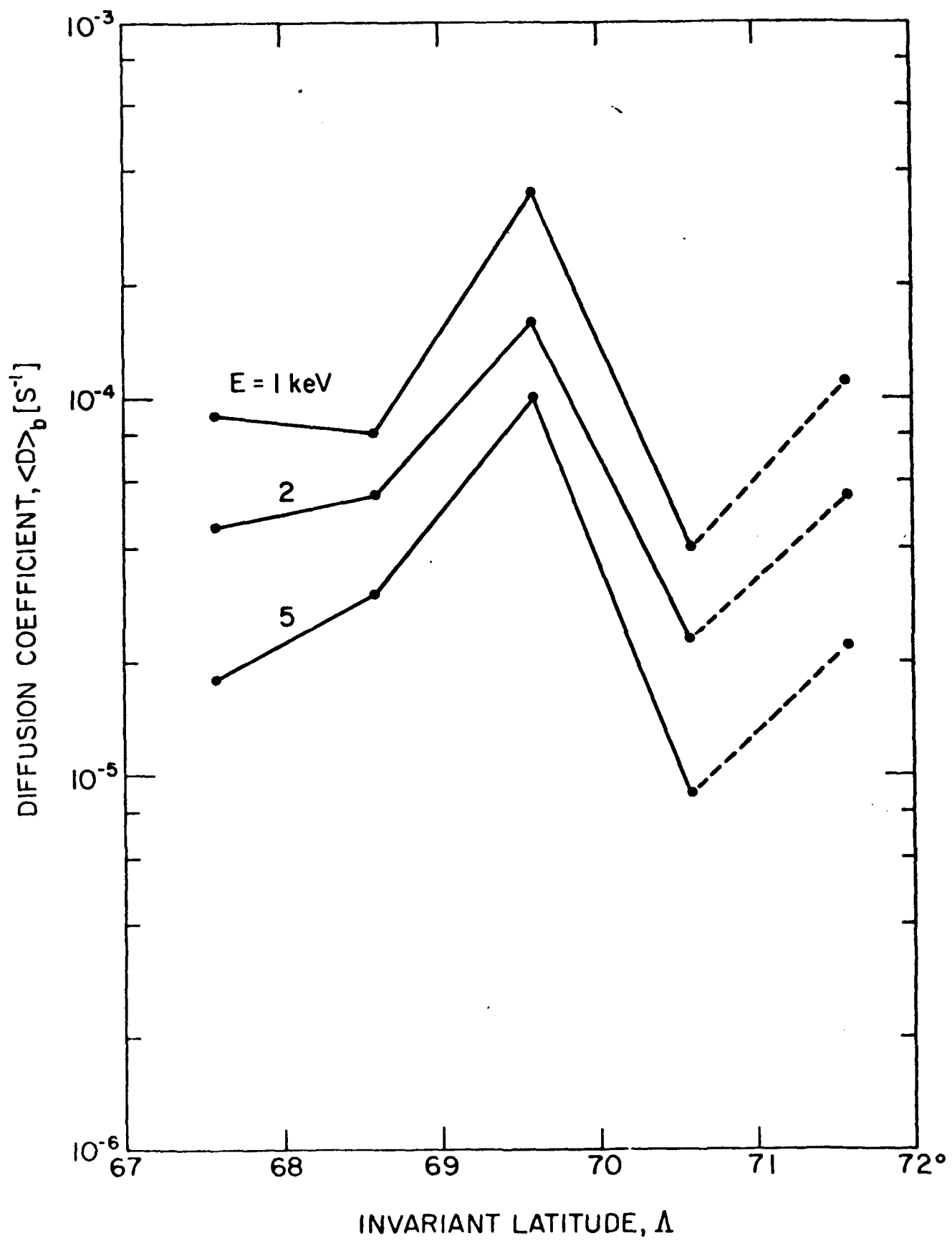


Figure III-4

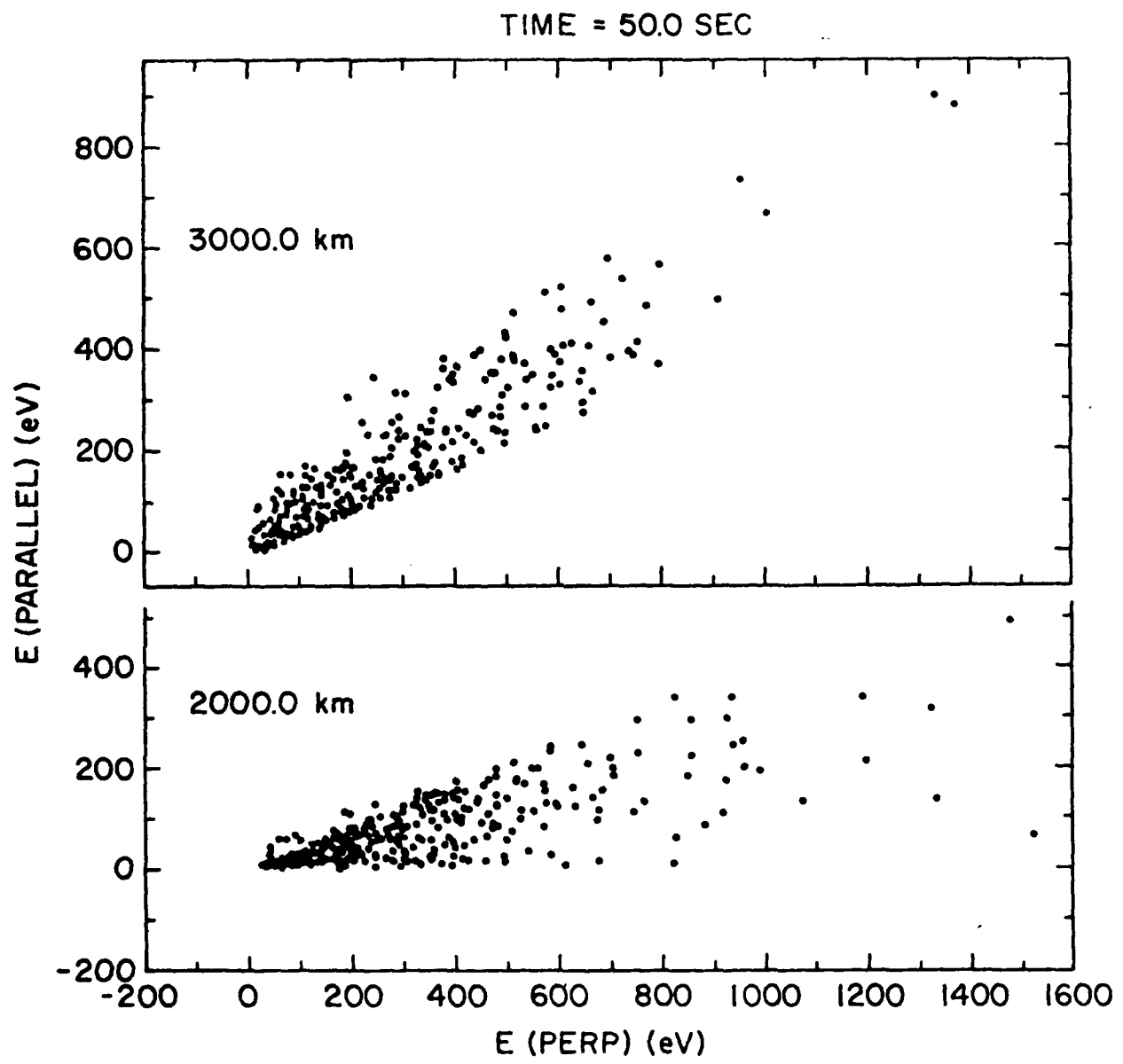


Figure III-5

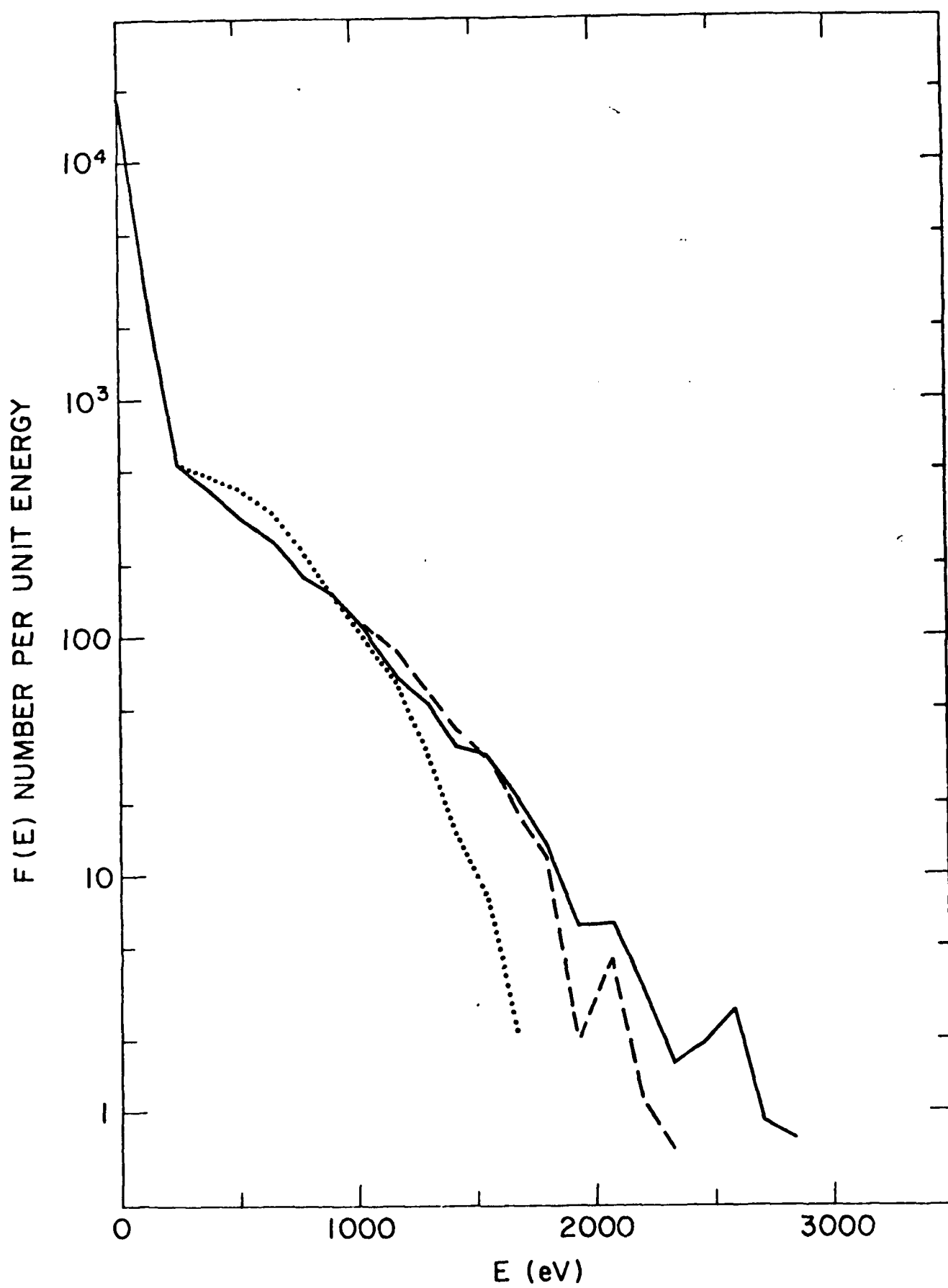


Figure III-6  
III-22

## IV. PROBE THEORY

### IV.1. Introduction

Probe theory has been an active area of research for almost two decades starting with the original study of Mott-Smith and Langmuir<sup>1</sup>. Earlier studies dealt mostly with the laboratory plasmas. With the advent of the space age, the theory had to be extended so that it can be applied to space plasmas as well. An interesting topic of space-related probe research is the spacecraft charging due to emission of positively charged particles. We are particularly interested in the experimental study by Cohen, Sherman and Mullen<sup>2</sup>. Their results on the variation of the extended probe-to-payload potential difference ( $\phi_t$ ) with respect to the electron density and to the beam current ( $I_0$ ) need to be explained analytically.

Since their observations indicated that the vehicle potential was independent of the neutral density and the vehicle pitch angle the effects of collisions and of the magnetic field seem to be unimportant. Thus, as a first attempt, it is reasonable to consider the collisionless, non-magnetic field electrostatic theories<sup>3,4,5</sup> to seek an explanation of the observed results. However, two important differences from these theories can be noted immediately: (i) the existence of the beam current and (ii) the different geometry of this problem. We can show that the observed saturation value of  $\phi_t$  can be explained in terms of fairly simple considerations.

The main difference that is expected to be due to beam emission is the limitation on the minimum value the probe potential can attain. (Positive ion emission makes the probe attain a negative potential  $\phi_p$  with respect to the ambient plasma). In the experiment<sup>2</sup>, the beam emission energy is ~2 keV. If  $\phi_p$  were to go below (-2) kV, the beam particles would not be able to escape, and this constitutes an obvious limit on  $\phi_p$ ,  $|\phi_p| \leq 2$  kV. As the beam current is increased,  $|\phi_p|$  would keep increasing until it reaches this saturation value. The extended probe is at a distance of 152 cm (taken perpendicular to the cylindrical axis of the probe). If the effective sheath were smaller than this distance, the extended probe potential  $\phi_t$  would reflect the ambient plasma potential (=0), and  $\phi_t = \phi_1 - \phi_p$  would be the same as  $(-\phi_p) = |\phi_p|$ . Under these conditions,  $\phi_t$  would also saturate at 2 kV. The observed value of ~1 kV suggests that only part of the potential drop occurs at a distance  $r_1$  such as

that of the extended probe, and the sheath size may be larger than this distance. A simple estimate for the sheath size  $r_o$  is obtained from the "free fall" condition  $I_o = r_o^2 n_0 v_t$  where  $n_0$  is the ambient charged particle density and  $v_t$  is the thermal velocity of the ions in the ambient plasma (beyond the sheath). For the parameters of this problem  $r_o \gg r_1$ , and the potential variation from the payload to the extended probe is essentially governed by the Laplace's equation since the charge term is negligible near the payload.

If we consider the rocket to be an idealized sphere, with radius  $r_p$ ,

$$\phi_p \sim \frac{1}{r_p}, \quad \phi_t \sim \frac{1}{r_1},$$

and the ratio

$$\rho = \frac{\phi_t}{|\phi_p|} = 1 - \frac{r_p}{r_1}.$$

This ratio is independent of the beam current or the saturation potential. For this experiment, depending on how one defines the equivalent sphere radius,  $r_p$ , we find  $\rho \approx 0.7$  to 0.75. This provides a saturation value for  $\phi_t \approx 1.4$  to 1.5 kV.

If we consider the rocket to be a long cylinder, and use the two-dimensional picture in its neighborhood,

$$\phi_p \sim B \ln(r_p/r_o), \quad \phi_1 \sim B \ln(r_1/r_o),$$

and the ratio

$$\rho = \frac{\ln(r_1/r_p)}{\ln(r_o/r_p)}.$$

Now the ratio depends mildly on the beam current through  $r_o$ . For the parameters of this experiment, one finds  $\rho \approx 0.5$  and the saturation value for  $\phi_t \approx 1$  kV, which is in good agreement with the observed value.

#### IV.2. Detailed Theory

It is rather remarkable that the above simplified picture, without any detailed matching of the near and far solutions and without using the charge term, gave such a good agreement with the experimental result. It is clearly important then to develop a more detailed theory of this phenomenon along these lines.

In order to develop a theory for the mixed geometry, it is helpful first to obtain a detailed understanding of the purely spherical and purely cylindrical situations. The first refers to a spherical probe and a spherical sheath, the second refers to an infinite cylindrical probe surrounded by a cylindrical sheath surface. While the basic differential equation for both cases and some analysis and numerical solutions in each case are already available in the work of Lam<sup>3</sup>, we have gone much beyond that effort and succeeded in obtaining very accurate analytical representations for the space potential. These results also allow us to develop a theory for the mixed geometry.

#### IV.2.1 Spherical Geometry

For the sheath region, in the notation of Lam<sup>3</sup>, the basic differential equation is

$$\tau^2 \frac{d^2 F}{d\tau^2} = \frac{1}{F^{1/2}} \quad (1)$$

where  $F$  is a scaled, dimensionless potential and  $\tau = r_1/r$  where  $r$  is the distance from the center of the probe and  $r_1$  is slightly larger than  $r_0$ , the free fall sheath size given by  $I_0 = \pi r_0^2 n_0 v_t e$ , where  $n_0$  is the ambient charged particle density,  $v_t$  the thermal velocity of the ions in the ambient plasma and  $I_0$  the beam current.

Lam<sup>3</sup> showed that

$$\lim_{\tau \rightarrow 1} F(\tau) = \left(\frac{3}{2}\right)^{\frac{4}{3}} (\tau-1)^{\frac{4}{3}} , \quad (2)$$

$$\lim_{\tau \rightarrow \infty} F(\tau) = 1.9\tau - 2.7 , \quad (3)$$

and also provided a table of numerical values for  $F(\tau)$  for  $\tau=1$  to  $\tau=10$ , and a graph of  $F(\tau)$  over a smaller range of  $\tau$ .

Introducing  $\tau=e^x$ ,  $x=\log \tau$  simplifies Eq.(1) to

$$F'' - F' = \frac{1}{\sqrt{F}} \quad (4)$$

where prime denotes differentiation with respect to  $x$ .

Obtaining a series solution for small  $x$  is straightforward; one finds,

$$F = a_0 x^{4/3} \left\{ 1 + b_1 x + b_2 x^2 + \dots \right\}, \quad (5)$$

$$a_0 = (3/2)^{4/3}, \quad b_1 = \frac{2}{5}, \quad b_2 = \frac{3}{25}, \quad b_3 = \frac{229}{8250}, \dots$$

Such a solution was also obtained recently by Leadon et al<sup>6</sup>, except that their coefficients were in the form  $A_1 = a_0$ ,  $A_2 = a_0 b_1$ ,  $A_3 = a_0 b_2$ , etc. and were expressed numerically in decimal form. Thus, the simple rational character of  $b_1$  and  $b_2$  was not recognized. We further noted that there were simple relations between successive coefficients.

$$b_2 = \frac{3}{10} b_1, \quad b_3 \approx \frac{3}{13} b_2, \quad b_4 \approx \frac{3}{16} b_3, \dots \quad (6)$$

which lead to a simplified, explicit equation for  $F$ ,

$$F' - F = g(x)$$

$$g(x) \approx \frac{4}{3} a_0 x^{1/3} \left\{ 1 - \frac{x}{20} \right\}. \quad (7)$$

An explicit solution in terms of incomplete gamma functions is thus obtained,

$$F(x) \approx \frac{4}{3} a_0 \left\{ \gamma^{4/3}(x) - \frac{1}{20} \gamma^{7/3}(x) \right\}. \quad (8)$$

The series solution (5) is not valid for large  $x$ , whereas (8) is well defined for all  $x$ . It was also found to be numerically accurate to within 8 parts per million for  $x \leq 1$  (when compared to the exact, numerically obtained  $F$ ). It can be shown also that for large  $x$ , the result is about  $\frac{1}{4}\%$  too low and it reduces to the form (3), with slightly different coefficients. In spite of all the success and convenience of the solution (8) it is still only a (good) approximation and one can seek iterative procedures that provide improvements.

Some exact results can be derived from (4), which by two integrations, and using the boundary conditions  $F(0) = 0$ ,  $F'(0) = 0$  can be converted to the integral

$$F = e^x \int_0^x e^{-x'} dx' \int_0^{x'} dx'' \frac{1}{\sqrt{F(x'')}} . \quad (9)$$

This leads to the exact result, for large  $x$ ,

$$F = Ae^x + B , \quad (10)$$

where

$$A = \int_0^{\infty} dx e^{-x} F^{-1/2}(x) , \quad (11)$$

$$B = - \int_0^{\infty} dx F^{-1/2}(x) . \quad (12)$$

An interesting procedure to evaluate  $A$  is to use the small- $x$  expansion (5) for  $F$  in (11); this leads to  $A \approx 1.913$  by keeping the first few terms in  $F$ . Thus we have shown that the small- $x$  expansion and the large- $x$  behavior of  $F$  are connected in a precise fashion. This is a fairly general result for the Poisson equation when the charge density term is a function of the potential.

An alternate approach to obtain the large  $x$  behavior of  $F$  is to assume a direct series expansion in inverse power of  $\tau$  to solve (1). Such a procedure was carried out by Leadon et al<sup>6</sup>; this method, however, cannot show the connection between the small- $x$  and large- $x$  behavior, as through (11) or (12). In fact, an auxiliary matching of the two series solutions in some intermediate domain of  $x$  becomes necessary, and the accuracy of determination of the coefficients of the large- $x$  series depends on how the matching is carried out. We use the large- $x$  series solution, and determine its two arbitrary constants  $A$  and  $B$  by exploiting (11) and (12).

It should be noted that (8) can be made more accurate by keeping higher order terms of  $g(x)$  in (7), and if we do so, the improved (8) precisely represents the large- $x$  behavior with the proper coefficients  $A$  and  $B$ .

In summary we have developed several new results for the spherical geometry, and a very accurate explicit solution has been provided for the poten-

tial. The methods developed are quite general and can be carried over to cylindrical geometry as shown below.

#### IV.2.2 Cylindrical Geometry

Now the basic differential equation, in the notation of Lam<sup>3</sup> is

$$\tau^2 \frac{d}{d\tau} (\tau \frac{dG}{d\tau}) = \frac{1}{G^{1/2}} \quad (13)$$

where  $G$  is a dimensionless, scaled potential. Lam provided a table and a graph for  $G$ , by numerical integration of (13) over a small range of  $\tau$ . Interestingly, as  $\tau \rightarrow 1$ ,  $G(\tau)$  has the same behavior as  $F$  in Eq. (2). Lam did not provide any analog of Eq. (3).

We have analyzed (13) by methods similar to the spherical case, and we find in terms of  $x = \ln \tau$ ,

$$G''' = \frac{e^{-x}}{\sqrt{G}} \quad , \quad (14)$$

$$G(x) = a_0 x^{4/3} (1 + b_1 x + b_2 x^2 + \dots) \quad , \quad (\text{small } x) \quad , \quad (15)$$

$$a_0 = (3/2)^{4/3} \quad , \quad b_1 = -\frac{2}{15} \quad , \quad b_2 = \frac{11}{450} \quad , \quad \dots \quad ,$$

$$G(x) = Ax + B + \dots \quad (\text{large } x) \quad , \quad (16)$$

$$A = \int_0^\infty dx e^{-x} G^{-1/2} \quad , \quad (17)$$

$$B = -\int_0^\infty dx x e^{-x} G^{-1/2} \quad . \quad (18)$$

Results (17) and (18) are exact, and if we use (15) to represent  $G$  in those equations, we find  $A \approx 2.09$  and  $B \approx -0.75$  from the first few terms in (15). We have also solved (13) directly in terms of a large  $x$  series of the form

$$G(x) = AX + B + \sum_{m=1}^{\infty} \sum_{n=0}^{\infty} c_{mn} e^{-mx} x^{-\frac{3m}{2} - n+1} \quad (19)$$

where A and B are already known from (17) and (18) and the constants  $c_{mn}$  are expressible in terms of A and B.

The accuracy of our results for the cylindrical case is comparable to that of the spherical case. Since Lam gave the numerical (exact) results for G for only a small range of  $\tau$ , we cannot ascertain this directly over a wider range. However, we have matched the small-x and large-x series and found that they agree very well in the intermediate domain. An analog of (8) for the potential in the cylindrical case can also be written down, but more terms are required for accuracy.

#### IV.2.3 Mixed Geometry

The more realistic problem of the space probes requires us to consider a cylindrical picture when  $r \ll l/2$ ,  $l$  being the length of the cylinder, a spherical picture when  $r \gg l/2$ , and the problem of matching. The simplest approach is to consider the plane of symmetry passing through the center of the cylinder and perpendicular to its axis. In this plane, one can use (19) for the small-r (large- $\tau$ ) solution and (5) or (8) for the large-r (small x) solution. This is a reasonable approximation, since the role of the charge term in the Poisson equation becomes quite weakened near the probe cylinder (i.e. for large  $\tau$ ), and only the first two terms in (19) representing a Coulomb potential and a fixed bias term are really important. Further improvements are obtained by keeping the next few terms in (19). While the structure of the solution is not changed, the numerical values of A and B are no longer as in (17) or (18). These have to be determined now by matching (19) and (5) over the intermediate domain at two points.

#### IV.3. Comparison with Experiments

The saturation value of  $\phi_t$ , in Figure 5 of Cohen et al<sup>2</sup> is well explained by our approach. The development of the theory for the mixed geometry allows us to obtain results for intermediate values of  $\tau$ , which provides a comparison with Figure 4 of their work.

It is clear from the geometry of the experimental set-up that the potential drop quite near the long cylindrical payload will be better described by the two-dimensional Laplace's equation. This seems to be borne out by the better agreement of  $\rho$  (2-dim) with the observed value. Another test of this picture would be to examine the variation of  $\rho$  with current  $I_0$ . Since  $r_0$  increases as  $I_0^{1/2}$ ,  $\rho$  (and  $\phi_t$ ) will decrease with increasing current beyond saturation. This can be easily tested if additional experimental data become available.

To understand the variation of  $\phi_t$  for the full range of  $I_0$ , we replotted that data on a log-log plot. We find that  $\phi_t$  increases only as  $\sim I_0^{1/4}$  in the low-current domain. This is to be contrasted with  $I_0^{7/6}$  for a Lam-type theory<sup>3</sup>. The two curves (observed data and Lam-type theory) cross at  $I_0 \sim 50\mu\text{A}$ ,  $\phi_t \sim 700\text{V}$ . One must explain why the observed curve remains above the Lam-theory for low currents and why it remains below the Lam-theory for high currents.

Since Lam-theory does not include beam emission, it does not lead to a saturation for  $\phi_p$ , and the increasing difference from the observed results for larger currents is due to this limitation of that theory. A modified theory, which takes into consideration the beam emission and the effect of the ion space charge in the emitted beam is required. We have calculated the amount of positive charge  $Q_+$  in the beam up to  $r_0$  and find it becomes comparable to  $Q_-$ , the total negative charge on the rocket, for high currents. Working out the electrostatics for this "tadpole" charge distribution might provide a smooth and gradual approach to saturation.

Another physical effect missing in Lam-type theories is the "trapped ion" effect. It has been shown that when the probe size is small compared to the sheath size, ion-trapping will occur and this will reduce the pull exercised by the negative charge of the rocket. This in turn will allow a build-up of a larger probe potential for the same beam current. This effect might explain why the observed potential is larger than the Lam-theory in the region of lower currents.

### References

- 1) Mott-Smith, H.M. and Langmuir, I., The theory of collectors in gaseous discharges, Phys. Rev., 28, 727, 1926.
- 2) Cohen, H.A., Sherman, C., and Mullen, E.G., Spacecraft charging due to positive ion emissions: An experimental study, Geophys. Res. Lett., 6, 515, 1979.
- 3) Lam, S.H., Unified theory for the Langmuir probe in a collisionless plasma, Phys. Fluids, 8, 73, 1965.
- 4) Bernstein, I., and Rabinowitz, I., Theory of electrostatic probes in a low density plasma, Phys. Fluids, 2, 112, 1959.
- 5) Laframboise, J.G., Theory of spherical and cylindrical Langmuir probes in a collisionless Maxwellian plasma at rest, UTIAS Report No. 100, University of Toronto, 1966.
- 6) Leadon, R.E., Woods, A.J., Wenaas, E.P., and Klein, H.H., Analytical investigation of emitting probes in an ionized plasma, FGL Report AFGL-TR-81-0138, ADA 104166, 1981.

**END**

**FILMED**

**8-85**

**DTIC**